Article

Developmental Cell

Metabolic Remodeling during Liver Regeneration

Graphical Abstract

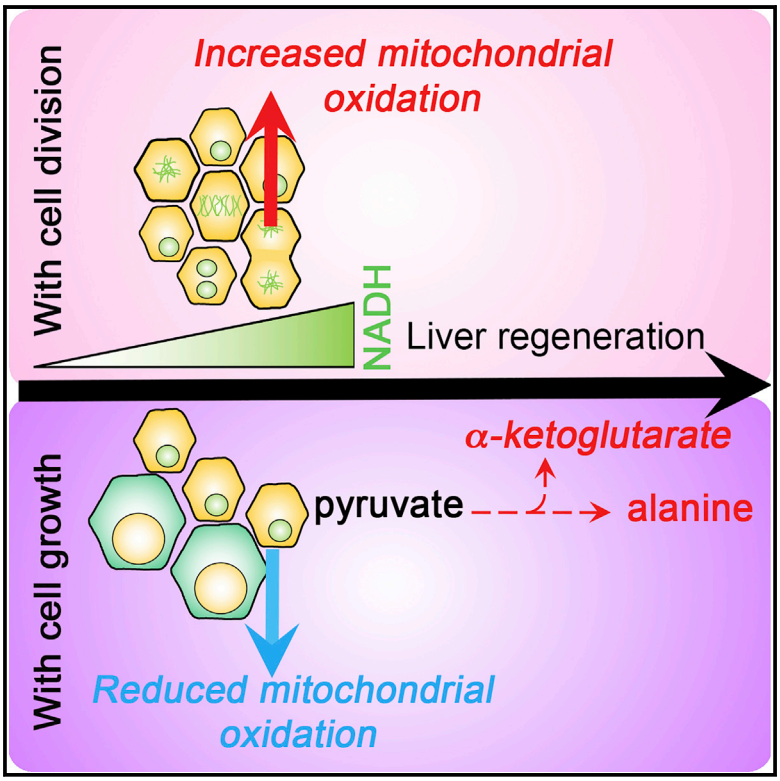

Authors

Matias J. Caldez, Noémi Van Hul, Hiromi W.L. Koh, ..., Hyungwon Choi, Mikael Björklund, Philipp Kaldis

Correspondence

22mtbx29@gmail.com

In Brief

In this work, Caldez et al. show that when liver cells are not able to divide during liver regeneration, they hyperactivate alanine transaminase (ALT), a signal of liver damage, that at the same time acts as an essential metabolic regulator required to support tissue recovery.

Highlights

- Decreased hepatic division during regeneration correlates with impaired metabolic homeostasis
- Impaired mitochondrial respiration/oxidation results in compromised metabolic homeostasis
- Non-dividing hepatocytes increase alanine transaminase flux during tissue repair

Caldez et al., 2018, Developmental Cell *47*, 425–438
November 19, 2018
https://doi.org/10.1016/j.devcel.2018.09.020

CellPress

Developmental Cell
Article

Metabolic Remodeling during Liver Regeneration

Matias J. Caldez,[1,2] Noémi Van Hul,[1] Hiromi W.L. Koh,[3] Xing Qi Teo,[4] Jun Jun Fan,[5,6,7] Peck Yean Tan,[8] Matthew R. Dewhurst,[1,9] Peh Gek Too,[8] S. Zakiah A. Talib,[1] Beatrice E. Chiang,[1] Walter Stünkel,[8] Hanry Yu,[5,11,12,13] Philip Lee,[4] Tobias Fuhrer,[10] Hyungwon Choi,[1,3] Mikael Björklund,[14] and Philipp Kaldis[1,2,15,*]

[1]Institute of Molecular and Cell Biology (IMCB), A*STAR (Agency for Science, Technology and Research), 61 Biopolis Drive, Proteos #3-09, Singapore 138673, Republic of Singapore
[2]National University of Singapore (NUS), Department of Biochemistry, Singapore 117597, Republic of Singapore
[3]Saw Swee Hock School of Public Health, National University of Singapore, 12 Science Drive 2, Singapore 117549, Republic of Singapore
[4]Singapore Bio-Imaging Consortium, A*STAR, Singapore, Republic of Singapore
[5]Institute of Bioengineering and Nanotechnology, A*STAR, The Nanos, #04-01, 31 Biopolis Way, Singapore 138669, Republic of Singapore
[6]Singapore-MIT Alliance for Research and Technology, 1 CREATE Way, #10-01 CREATE Tower, Singapore 138602, Republic of Singapore
[7]Department of Orthopaedic Surgery, Xi Jing Hospital, Fourth Military Medical University, #88 Jiefang Road, Xi'an 710032, China
[8]Singapore Institute of Clinical Sciences, A*STAR, Singapore, Republic of Singapore
[9]Faculty of Biology, Medicine and Health, University of Manchester, AV Hill Building, Oxford Road, Manchester M13 9PT, UK
[10]Institute of Molecular Systems Biology, ETH Zürich, Zürich, Switzerland
[11]Department of Physiology, Yong Loo Lin School of Medicine, MD9-04-11, 2 Medical Drive, Singapore 117597, Republic of Singapore
[12]Mechanobiology Institute, National University of Singapore, 5A Engineering Drive 1, Singapore 117411, Republic of Singapore
[13]Gastroenterology Department, Southern Medical University, Guangzhou 510515, China
[14]Zhejiang University-University of Edinburgh (ZJU-UoE) Institute, Zhejiang University School of Medicine, International Campus, Zhejiang University, 718 East Haizhou Rd, Haining, Zhejiang 314400, China
[15]Lead Contact
*Correspondence: 22mtbx29@gmail.com
https://doi.org/10.1016/j.devcel.2018.09.020

SUMMARY

Liver disease is linked to a decreased capacity of hepatocytes to divide. In addition, cellular metabolism is important for tissue homeostasis and regeneration. Since metabolic changes are a hallmark of liver disease, we investigated the connections between metabolism and cell division. We determined global metabolic changes at different stages of liver regeneration using a combination of integrated transcriptomic and metabolomic analyses with advanced functional redox *in vivo* imaging. Our data indicate that blocking hepatocyte division during regeneration leads to mitochondrial dysfunction and downregulation of oxidative pathways. This resulted in an increased redox ratio and hyperactivity of alanine transaminase allowing the production of alanine and α-ketoglutarate from pyruvate when mitochondrial functions are impaired. Our data suggests that during liver regeneration, cell division leads to hepatic metabolic remodeling. Moreover, we demonstrate that hepatocytes are equipped with a flexible metabolic machinery able to adapt dynamically to changes during tissue regeneration.

INTRODUCTION

Coordinated regulation of metabolism and cell division during tissue renewal and regeneration is a prerequisite for tissue recovery after injury (Locasale and Cantley, 2011). Despite recent advances in understanding metabolic requirements of proliferating cells, most research done has focused on cells that display abnormal cell divisions, i.e., tumor-derived cell lines (Vander Heiden et al., 2009). Currently, little is known about metabolic changes during innate tissue regeneration. In mammals, regeneration is important for tissue homeostasis, particularly in tissues such as the liver, which are constantly exposed to cellular damage (Fausto et al., 2006). In the adult liver, hepatocytes are quiescent yet perform a wide range of demanding metabolic functions (Huang and Rudnick, 2014). In contrast, when confronted with damage, hepatocytes undergo one or more rounds of cell division inducing a compensatory hyperplastic response, better known as liver regeneration (Fausto et al., 2006). Liver regeneration is divided into three phases: (1) initiation phase—characterized by activation of transcription factors to promote hepatocyte division; (2) progression phase—characterized by DNA replication and hepatic division; and (3) termination phase—with a balance of cell division and apoptosis to control organ size. Although a lot is known about the transcriptional program that characterizes each phase of liver regeneration (Fausto et al., 2006), there are scarce data about the regulation of metabolism, the metabolic needs of dividing hepatocytes, and what happens to metabolic homeostasis when hepatocyte division is impaired. Since impaired division of hepatocytes is a common feature of many liver diseases (Forbes and Newsome, 2016), including metabolic disorders (DeAngelis et al., 2005; Veteläinen et al., 2007), understanding the metabolic needs of dividing hepatocytes during regeneration has direct clinical implications.

Analysis of gene expression data previously implied that metabolic genes are suppressed during liver regeneration (Fausto et al., 2006). This seems paradoxical because after injury, the liver has to maintain metabolic homeostasis and at the same

time support regeneration. Thus, understanding the metabolic adaptation of regenerating hepatocytes offers a unique opportunity to dissect the underlying mechanism of how cell division and metabolism interact during tissue repair. Moreover, investigating the metabolic regulation during regeneration would help to discover novel metabolic pathways that could be potentially useful to promote resolution of the damage. Surprisingly, cell division seems to be dispensable to recover organ size after partial hepatectomy (PHx) because hepatocytes increase in size (Diril et al., 2012; Haga et al., 2005; Minamishima et al., 2002). This model of tissue renewal by increased cellular size is known as compensatory cellular hypertrophy (CCH) and has been suggested to be a robust model by which organs recover from injury in species ranging from flies to mammals (Tamori and Deng, 2014). Using a mouse model with hepatocyte-specific deletion of cyclin-dependent kinase 1 (Cdk1), a major regulator of cell division, we demonstrated that hepatocytes do not divide but increase in size after liver resection (Diril et al., 2012), suggesting that this may be a good model to study tissue regeneration by CCH. We also uncovered that increased nuclear size was correlated with decreased expression of genes with mitochondrial functions and increases in markers of aerobic glycolysis (Miettinen et al., 2014). These initial results suggested that tissue regeneration by CCH is associated with remodeling of oxidative pathways.

Aiming to assess the dynamic changes in metabolism during tissue repair, we investigated metabolic pathways using *in vivo* molecular imaging techniques in combination with metabolomic and transcriptomic analyses. We found that regeneration is accompanied by reduced oxidative metabolism, which in CCH cells was due to diminished mitochondrial metabolism. Integrated analysis of transcriptomic and metabolomic data validated the observed metabolic remodeling during liver regeneration. Functional MRI was used to measure the activity of hepatic enzymes involved in pyruvate oxidation, and we observed that as a consequence of mitochondrial impairment, hepatocytes favor the conversion of pyruvate to alanine by increasing the metabolic flux through alanine transaminase (ALT). We uncovered that cell division and metabolism are interlinked during regeneration. Our innovative approach of combining functional metabolic imaging with metabolomic and transcriptomic analyses reveals potential clinical applications to assess liver physiology after acute liver damage.

RESULTS

Physiologic Consequences of Liver Regeneration on Cellular and Organismal Levels

Although liver regeneration has been studied extensively on many levels (Forbes and Newsome, 2016), an analysis of metabolic regulation has not been done. To study the metabolic requirements of tissue regeneration *in vivo*, we used a mouse model of resection of 2/3 of liver mass (PHx). We analyzed well-defined time points during liver regeneration, chosen considering three criteria: (1) the stage of the regeneration process; (2) metabolic demands; and (3) the cell cycle phase of hepatocytes. During the initiation phase of liver regeneration, hypertrophy of hepatocytes dominates, while at later stages, regeneration depends mostly on cell division (Miyaoka et al., 2012). Therefore, the time points chosen aimed to differentiate the physiological changes that correlate with hypertrophy from those correlating with cell division; thus, we collected liver at 8 hr, 36 hr, 96 hr, and 168 hr after PHx (Figure 1A).

To understand changes in hepatocyte size during the regeneration process, cryo-sections were stained with phalloidin and DAPI to visualize cell and nuclear morphology (Figure 1B). Measurements of hepatocyte size (defined by the circumference of a hepatocyte outlined by the phalloidin stain) indicated an increase in cell size during liver regeneration. Cell size peaked at 36 hr after PHx (44% increase compared to 0 hr) and returned to baseline in the termination phase (Figures 1C and S1A–S1E), confirming that hypertrophy contributes in the early time points as previously suggested (Miyaoka et al., 2012). Interestingly, at 36 hr after PHx, which is the peak of DNA replication and cell division, the cell size distribution indicated the presence of two populations of hepatocytes (Figure 1D), which were not observed at any other time point (for a detailed quantification of the frequency, see Figures S1A–S1E), potentially indicating a heterogeneity of the hepatocyte population.

To study cell cycle progression, we determined the expression of two important genes, cyclin-dependent kinase 1 (Cdk1) and a negative regulator of Cdk1, cyclin-dependent kinase inhibitor 1A ($p21^{CIP1/WAF1}$) (el-Deiry et al., 1993). Cdk1 is an essential kinase required for cell division, and its deletion prevents division of hepatocytes (Diril et al., 2012; Santamaría et al., 2007). *Cdk1* mRNA levels peaked at 36 hr and returned to baseline by 168 hr (Figure 1E), which is consistent with CDK1 protein levels (Diril et al., 2012), suggesting that cell division is important during this time frame. In contrast, mRNA expression of $p21^{CIP1/WAF1}$ was increased at 8 hr after PHx and remained at lower levels during the peak of DNA replication at 36 hr after PHx (Figure 1F). $p21^{CIP1/WAF1}$ is usually increased in liver disease (Richardson et al., 2007), suggesting that the Cdk1-p21 axis may have an important role in the response to liver damage.

We then used blood serum to measure total ALT and glucose levels, two surrogate markers of liver damage and metabolism, respectively (Eguchi et al., 2014). We observed a 24-fold increase in ALT at 8 hr after PHx compared to 0 hr, which gradually returned to the initial level (Figure 1G). We also noted a less than 2-fold decrease in total glucose at the initiation phase of liver regeneration (8 hr) before it returned to levels of 0 hr at the end of the time course (Figure 1H). These results support the idea that changes in transaminases and glucose metabolism accompany liver regeneration. Since hypoglycemia and hyper-transaminemia are markers of liver damage (Eguchi et al., 2014) and Cdk1 is a kinase essential to maintain the self-renewal of hepatocytes, these results encouraged us to study potential links between the expression of Cdk1, cell division or hypertrophy, metabolic remodeling, and liver damage in the regenerating liver.

Transcriptomic Analysis Combined with *In Vivo* Molecular Imaging Uncover Changes in Biological Oxidations during Liver Regeneration

In order to study the pathways involved in liver regeneration, we determined changes in mRNA expression using RNA sequencing (RNA-seq) at the time points mentioned above (Figure 1A). mRNA expression levels were compared between each time point during liver regeneration at 0 hr (before PHx) and after

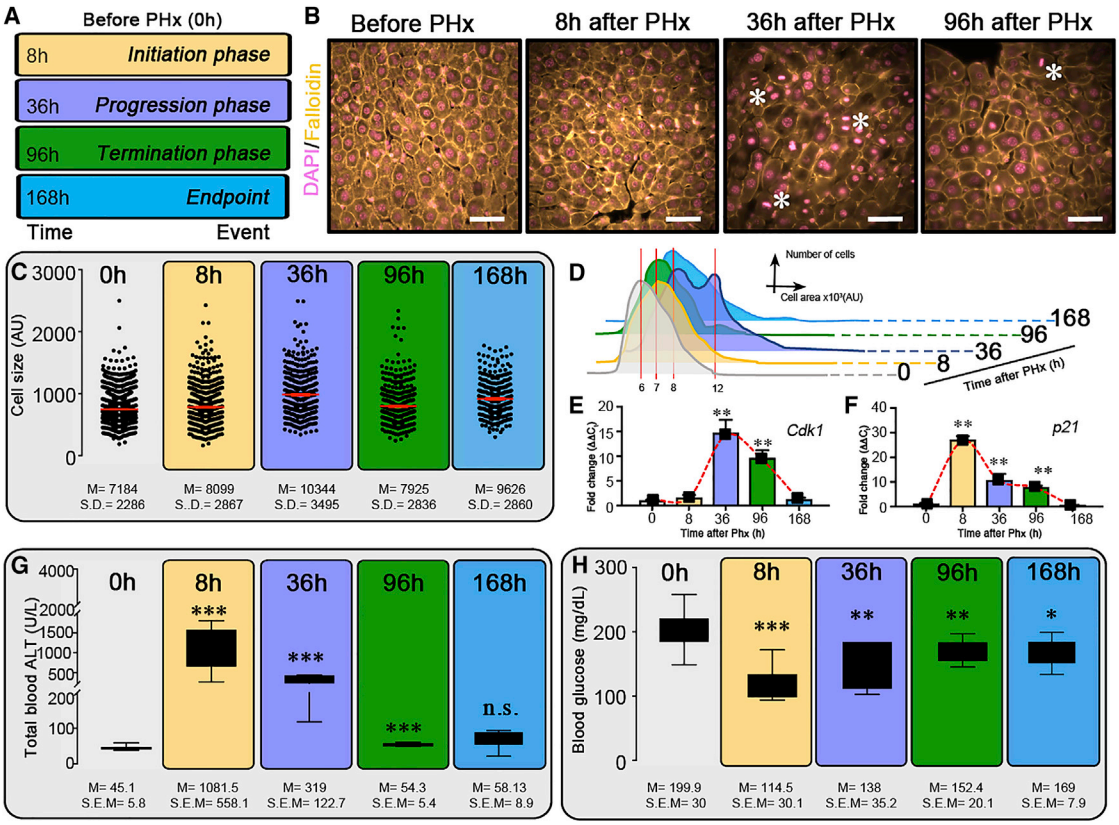

Figure 1. Physiology of the Regenerating Liver in Wild Type Mice

(A) Time points during liver regeneration selected in this study.

(B) Representative immunofluorescence images of liver sections displaying nuclei (magenta, DAPI) and actin (yellow, phalloidin); asterisks are mitotic figures, bars represent 50 μm (micrometers).

(C) Measurement of hepatocyte size during regeneration; each dot symbolizes one cell.

(D) Frequency of cell size at different time points during regeneration as a function of time and total number of cells.

(E and F) The mRNA expression of *Cdk1* and *p21*$^{Cip1/Waf1}$ was determined by qPCR (mean values and SEM) during liver regeneration.

(G and H) (G) ALT in units per liter (U/L) and (H) blood glucose in milligrams per deciliters (mg/dL) was determined in WT mice before and after partial hepatectomy.

M, mean; SEM, standard error of the mean; SD, standard deviation; BW, body weight; ALT, alanine transaminase; PHx, partial hepatectomy.

PHx. Correlation analysis between different time points to 0 hr reflected that a specific subset of genes displayed changes at respective time points during liver regeneration, without major reshuffling of the overall transcriptome and devoid of major transcriptomic differences among different batches of mice (Figure S1F). Moreover, t-distributed stochastic neighbor embedding (t-SNE) analysis clustered specific groups of mRNAs that were up- or downregulated at 8 hr, 36 hr, and 96 hr (Figure S1G). This confirmed that we were working with a solid dataset to understand global changes underlying regeneration.

The statistically significant changes in mRNA expression were grouped into ~60 pathways (Figure S1H), of which 24 contained the most representative set of genes (Figure 2A; for details of the analysis, refer to STAR Methods and Figure S1). We detected pathways previously described during liver regeneration including activation of transcription, inflammation, and others (Fausto et al., 2006) (Figures 2 and S2). However, cell cycle (peaked at 36 hr) and specific metabolic pathways such as biological oxidations were the most significant. Since it has been suggested that 2/3 liver resection results in significant reduction of glycogen content, with oxidation becoming an important source of metabolites and energy (Huang and Rudnick, 2014), the observation of reduction in biological oxidations was striking. Our transcriptomic data indicated a significant increase in oxidative stress only at 8 hr (Figure S1G), although "biological oxidations" were downregulated at all time points (Figure 2A). Based on this, we hypothesized that during regeneration, different oxidative processes may play distinctive roles.

Due to the limitations to determine functional changes in oxidative metabolism by gene expression data, we used intravital imaging to characterize metabolism in live animals. To do so, we measured autofluorescence of the redox coenzymes NADH and FAD, as previously described (Skala et al., 2007). FAD and NADH are cellular electron carriers during energy production, and the FAD-to-NADH ratio is used as an indicator of the cellular metabolic status. Since intravital imaging during liver regeneration has not been reported, we developed a new protocol of liver surgery that allowed us to (1) attach the abdominal imaging window to the mouse liver; and (2) image metabolite autofluorescence and tissue structure in real time in living mice

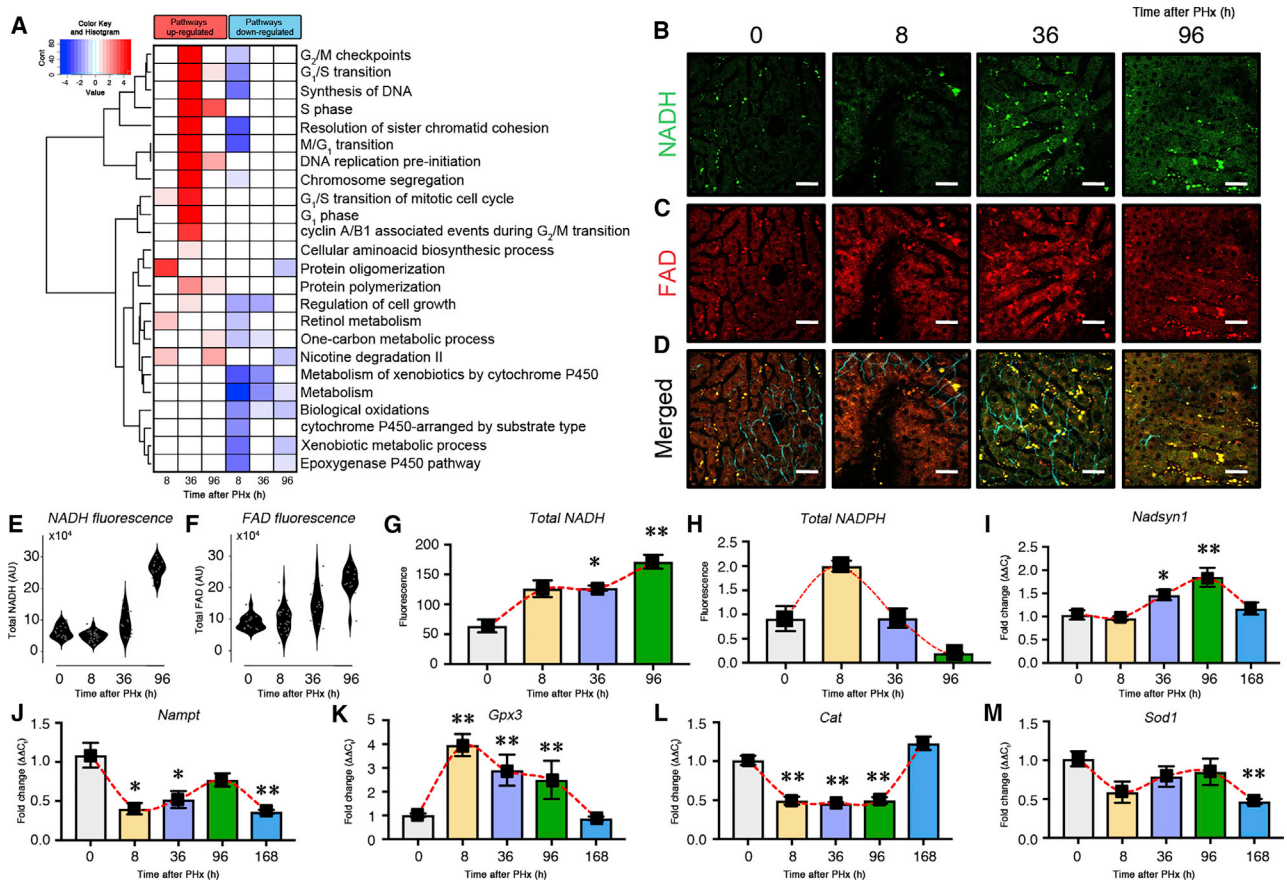

Figure 2. Hepatocyte Division during Liver Regeneration Is Accompanied by Increased Levels of NADH and FAD

(A) Heatmap with pathways from RNA sequencing analysis of WT livers.

(B–D) Representative images of NADH (B), FAD (C), and merged (D) measured with two-photon fluorescence microscopy obtained before and after liver resection; bars represent 120 μm.

(E and F) Violin plots with quantification of NADH (E) and FAD (F).

(G and H) Bar graphs with median values and SEM for total (G) NADH and (H) NADPH quantified from de-proteinized liver samples.

(I–M) mRNA expression of central enzymes involved in *de novo* NADH synthesis, *Nadsyn1* (I) and *Nampt* (J), or in oxidative stress response (K–M), *Gpx3*, *Cat*, and *Sod1* (median and SEM) was determined by qPCR during liver regeneration.

(Figure S2; for a detailed description of the surgical protocol, refer to STAR Methods). NADH increased steadily during liver regeneration, suggesting that NADH plays a role in hepatic division and tissue recovery (Figure 2B). This was corroborated by quantification of total NADH using image analysis (Figure 2E). Total FAD displayed a similar trend (Figures 2C and 2F), although less pronounced. We validated these observations by quantifying total NADH (Figure 2G) and NADPH (Figure 2H) from de-proteinized samples using biochemical assays. NADH displayed a steady increase during liver regeneration, while there was a peak of NADPH at 8 hr that was later reduced. These results suggest that intravital imaging is useful to measure redox equivalents during tissue regeneration and NADH may play a dominant role over NADPH under these conditions in wild-type (WT) animals.

To test whether there was a significant contribution from newly produced NAD^+ during regeneration, we measured the gene expression of glutamine-dependent NAD^+ synthase (*Nadsyn1*) and nicotinamide phosphoribosyltransferase (*Nampt*) (Figures 2I and 2J), two enzymes involved in *de novo* biosynthesis and salvage pathways of NAD^+, respectively. Both peaked at 96 hr, suggesting that increased NAD^+ production may be one of the reasons for increasing NADH levels at that time point. As mentioned previously, oxidative stress has been associated with changes in redox metabolism and as an initial signal to promote liver regeneration (Dragin et al., 2006; Vendemiale et al., 1995). We observed a transient increase in expression of glutathione peroxidase (*Gpx3*) at 8 hr, which correlated with a peak in NADPH (Figure 2K), while catalase (*Cat*) and superoxide dismutase (*Sod1*) (Figures 2L and 2M) mRNA levels were mostly reduced. Taken together, these results suggest that biological oxidations may play different roles during liver regeneration: oxidative stress is required in the initial stages of regeneration (based on expression of *Gpx3* and a peak of NADPH in Figure 2K), and increases in NADH correlate with the progression of liver regeneration and resolution of tissue damage at later time points. Presumably, these changes in oxidative metabolism reflect the metabolic needs of hepatocytes that undergo division. Based on this, we hypothesized that increases in NADH

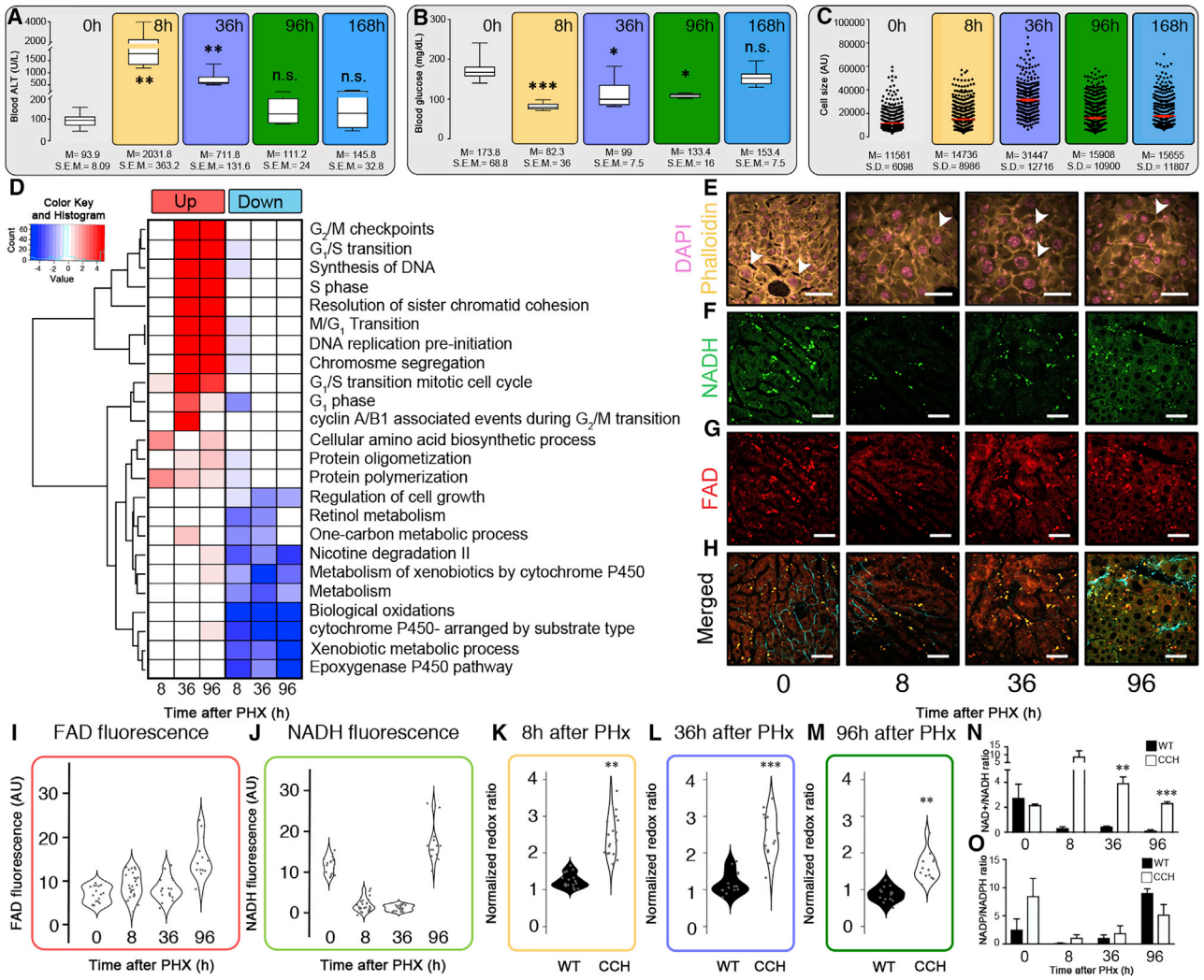

Figure 3. Tissue Regeneration by Compensatory Cellular Hypertrophy Occurs with a Significant Reduction in Oxidation

(A and B) (A) Blood ALT levels in units/liter (U/L) and (B) total blood glucose levels in mg/dL were determined from CCH mice during liver regeneration.

(C) Quantification of cell area of CCH hepatocytes.

(D) Pathway analysis of transcriptomic data at different time points during liver regeneration in CCH livers.

(E) Representative images of CCH liver stained with phalloidin and DAPI; arrows denote increases in cell size due to compensatory cellular hypertrophy; bars represent 50 μm.

(F–H) Representative images of NADH (F) and FAD (G) and merged (H, with collagen in cyan) images of regenerating liver using two-photon microscopy analysis are shown; bars represent 120 μm.

(I–M) Violin plots for quantification of total fluorescence of FAD (I) and NADH (J) and normalized redox ratio (K–M) of WT and CCH livers at different time points during liver regeneration.

(N and O) (N) NAD^+/NADH and (O) $NADP^+$/NADPH ratio was calculated for WT and CCH liver during liver regeneration.

are required to promote tissue regeneration. To further test this idea, we used a genetic mouse model in which we uncoupled cell division and hypertrophy.

Inhibition of Hepatocyte Division Results in Reduced Oxidative Metabolism and Increased Redox Ratio

Hepatic division is reduced and cell size is increased in several mouse models for liver disease (Forbes and Newsome, 2016). Moreover, there might be a direct or indirect connection between metabolism and cell division, since in mouse models with metabolic disorders, hepatocyte division is reduced (DeAngelis et al., 2005; Veteläinen et al., 2007) and $p21^{Cip1/Waf1}$ is often expressed at high levels (Richardson et al., 2007). We thus chose a direct approach by knocking out *Cdk1* in hepatocytes. $Cdk1^{flox/flox}$ was crossed with mice carrying the Albumin-cre recombinase (for details, see STAR Methods). $Cdk1^{Liv-/-}$ mice are viable and due to the block of cell division, display significant hypertrophy in hepatocytes (Diril et al., 2012). These mice, designated as CCH, underwent PHx, and blood glucose levels, ALT, and the size of hepatocytes were measured.

Before PHx, ALT was increased ≈2-fold in CCH mice compared to WT (Figures 3A and 1G) and peaked at 8 hr after

PHx before returning to baseline by 96 hr. However, at each of the time points, the levels of ALT were higher in CCH, suggesting that liver injury was more pronounced in CCH than in WT mice. Blood glucose levels in CCH mice were reduced more prominently than in WT mice and remained lower throughout regeneration before reaching near to normal levels by 168 hr (Figures 3B and 1H). Moreover, image analysis indicated a 3-fold increase in cell size at 36 hr compared to WT (Figures 3C, 3E, and S3F–S3J). The liver-to-body-size ratio was comparable in CCH and WT mice during the regenerative process (Figures S3A and S3B), suggesting that CCH mice recovered normal liver mass as shown before (Diril et al., 2012). We conclude that liver regeneration by CCH completes with increased markers of liver damage. We then hypothesized that while hypertrophy is sufficient to complete regeneration, it may be associated with significant remodeling of the metabolism.

In order to uncover the underlying causes for the changes in physiology of CCH mice, similar transcriptomic analysis as for WT liver was done (Figures S3C–S3E). In the pre-PHx samples, we found 848 genes (6.3%) with a ratio of median expression changes greater than 2-fold and 2,305 genes (17%) with changes greater than 1.5-fold in CCH compared to WT, with the majority of the changes occurring in the low abundance range. In other words, the expression levels did not change significantly for the majority of the genes between WT and CCH, suggesting that basic processes were maintained. This was supported by a principal-component analysis (PCA) of the mRNA expression levels, which clustered samples by time points during regeneration rather than by genotype (Figure S6A). Gene Ontology (GO) analysis of significantly altered genes allowed grouping in 60 pathways (before PHx compared to 8, 36, and 96 hr after PHx), with 24 pathways containing at least 15% of the genes in each pathway. The most upregulated pathways were associated with cell cycles at 36 hr and 96 hr after PHx (Figures 3I and S3D), in contrast to WT liver samples, in which those genes returned to baseline at the latter time point (Figure 2A). This is most likely due to the fact that hepatocyte division is blocked and cells are arrested in the G2 phase (Diril et al., 2012). The majority of downregulated pathways were enriched for metabolism, especially for oxidative pathways (Figure 3D), which was substantially more pronounced in CCH than in WT liver.

To further validate the reduction in oxidative metabolism, we used intravital imaging (Ritsma et al., 2013) in CCH liver following the same protocol as for WT and quantified the levels of NADH and FAD by autofluorescence (Figures 3E–3H). While FAD (Figure 3I) increased slightly during the time course, NADH decreased significantly at 8 hr and 36 hr but recovered at 96 hr (Figure 3J). Since the levels of FAD and NADH alone have limited biological significance, we calculated the redox ratio (Figures S2K and S2L) as defined previously (Skala et al., 2007). This ratio allows to deduce the rate of NADH oxidation. In this sense, when the TCA cycle increases relative to the rate of NADH oxidation, reduced redox equivalents become limited. Consequently, glycolysis and/or the Krebs cycle increase favoring biosynthesis relative to oxidative phosphorylation, which normally causes accumulation of NADH and a lower redox ratio (Quinn et al., 2013). In contrast, lower NADH autofluorescence and/or increased FAD autofluorescence may imply energetic stress, with elevated demands for energy (Georgakoudi and Quinn, 2012) increasing the redox ratio. When we determined the redox ratio in liver imaged during regeneration compared to before (0 hr), we observed a value close to 1 in WT liver, suggesting that there is redox homeostasis (Figures 3K–3M), despite the reduction in biological oxidations (Figure 2). In contrast, the redox ratio in CCH liver was significantly higher (Figures 3K–3M). Although additional production of NAD^+ could be a significant source for the elevated NADH levels, reduction to NADH in the cell originates mainly from mitochondrial metabolism. To study the source of oxidative changes, we then measured the conventional NAD^+/NADH and $NADP^+$/NADPH ratios (Figures 3N and 3O). Interestingly, the NAD^+/NADH ratio was reduced in WT mice during regeneration compared to the 0-hr time point, suggesting active mitochondrial metabolism to support liver regeneration (Figure 3N). Instead, the ratio of $NADP^+$/NADPH was reduced at 8 hr and 36 hr but increased $\approx$3-fold at 96 hr (Figure 3O). In contrast, in CCH livers, the NAD^+/NADH ratio was significantly elevated (Figure 3N), suggesting that reduced oxidative metabolism may be associated with impaired mitochondrial metabolism. Therefore, we set out to understand the molecular mechanisms that lead to the reduction in oxidative metabolism and whether there are compensatory pathways that may be correlated to tissue regeneration when hepatocyte division is impaired.

Tissue Regeneration by CCH Results in Reduction of Mitochondrial Functions

The current understanding is that mitochondrial oxidative metabolism is the most efficient way to produce metabolites and energy required for all cellular processes underlying liver regeneration (Smeitink et al., 2006). Since one of the main sources of NADH and FAD is the mitochondrial electron transport chain (ETC) (Feher, 2012), we hypothesized that tissue regeneration by CCH is impaired and liver may not regenerate at the same rate as WT livers. However, the rate of liver regeneration was not majorly impaired (Figures S3A and S3B). In other words, liver regeneration by CCH completes even in the presence of a significant reduction in oxidative pathways.

To study this further, we first analyzed whether regeneration by CCH is accompanied by changes in mitochondrial metabolism. We had previously shown that the number of mitochondria is similar in CCH compared to WT mice (Miettinen et al., 2014), and therefore we studied mitochondrial functions. We initially determined the levels of OXPHOS proteins, characteristic for each complex of the ETC (Figures 4A and S4A). Significant changes were observed in protein levels from several complexes, including complex II, succinate dehydrogenase B (SDHB) in both WT (Figure 4B) and CCH (Figure 4C) especially at 8 hr and 36 hr after PHx. This suggested that changes in oxidative metabolism might be related to fluctuations in expression of ETC complexes. This was of particular interest since SDHB protein levels seem to positively correlate with NADH fluorescence in the WT liver (Figure 4D). SDHB is the only enzyme involved in both TCA and OXPHOS metabolism and therefore a central enzyme in mitochondrial reactions (Rutter et al., 2010; Tretter et al., 2016).

Based on this, we then determined parameters of mitochondrial respiration using Seahorse analysis of isolated primary

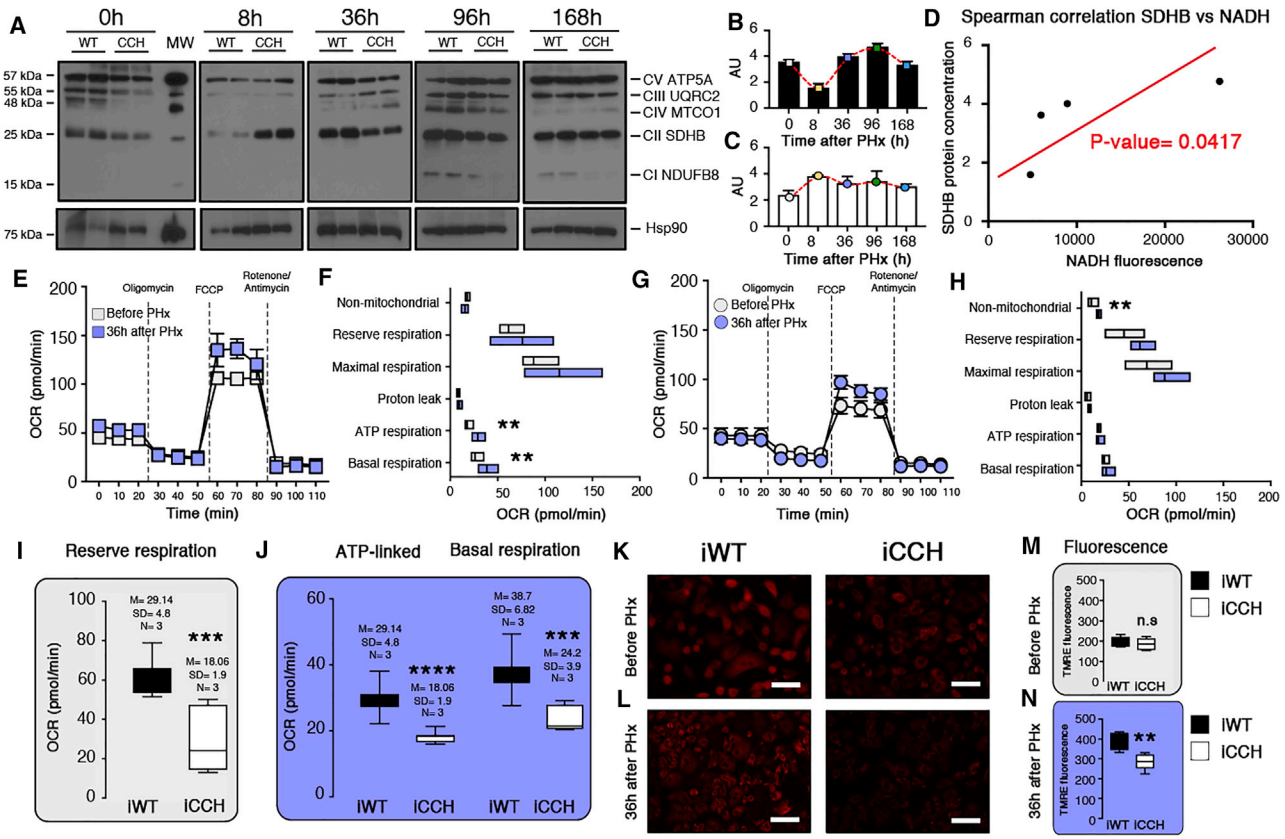

Figure 4. Tissue Regeneration by CCH Correlates with Impaired Mitochondrial Metabolism

(A) Western blots from liver lysates probed for the expression of OXPHOS proteins. Bar graphs with mean value with SEM quantification of western blots for SDHB protein regeneration in WT (B) and CCH (C) livers. AU refers to the percentage of area under the curve of the peaks measured from RGB intensity quantification.

(D) Spearman correlation between expression of SDHB and NADH levels measured by TPFM.

(E and G) Measurements of oxygen consumption rates (OCRs) in iWT (E) and iCCH (G) hepatocytes before and at 36 hr after liver resection. Each point represents the mean value with SEM.

(F and H) Components of mitochondrial respiration before and at 36 hr after PHx in WT (F) and CCH (H) hepatocytes.

(I) Reserve and (J) ATP-linked and basal respiration measured in WT and CCH hepatocytes before and after PHx.

Representative images and fluorescence quantification of TMRE before PHx in iWT (K) and iCCH (L) hepatocytes; bars represent 40 μm.

Whisker plots represent TMRE fluorescence before PHx (M) and 36 hr after PHx (N).

SDHB, succinate dehydrogenase; TPFM, two-photon fluorescence microscopy; iWT, inducible wild-type; iCCH, inducible compensatory cellular hypertrophy; OCR, oxygen consumption rate; TMRE, tetramethylrhodamine ethyl ester.

hepatocytes. However, isolated hepatocytes from *Cdk1*$^{Liv-/-}$ mice displayed significant reduction in viability (Figure S4B), and they appeared unhealthy (not shown). To circumvent this problem, we used *Cdk1*$^{flox/flox}$ mice crossed with tamoxifen-inducible Albumin-creERT2 mice. Hepatocytes were isolated 5 days after tamoxifen injection, which resulted in increased viability (Figure S4C) as well as substantially better general health of the cells (Figure S4D). Hepatocytes from WT animals will be called "inducible wild-type" (iWT), and those from the *Cdk1*$^{flox/flox}$ allele will be called "inducible compensatory cellular hypertrophy" (iCCH). These cells were then used to determine the oxygen consumption rate (OCR) before and at 36 hr after liver resection. We observed that in iWT hepatocytes, there was a significant increase in OCR at 36 hr after PHx (Figure 4E), which correlated with increases in all of the components of mitochondrial respiration (Figure 4F). In contrast, iCCH hepatocytes displayed no increase in OCR 36 hr after PHx (Figure 4G) with mostly unchanged parameters of mitochondrial respiration (Figure 4H). This suggests that the transition from a quiescent state (before PHx) to a proliferative state (peak of DNA replication) of WT hepatocytes is accompanied by increases in OCR. In contrast, because CCH hepatocytes do not proliferate due to the loss of *Cdk1*, they require alternative metabolic changes. When comparing OCR values between iWT and iCCH hepatocytes (Figures S4E and S4F), we observed significant reductions in the reserve respiratory capacity before PHx (Figure 4I), suggesting an impaired ability of iCCH hepatocytes to respond to energy stress. Similar findings have been previously described in other types of cells (Miettinen and Björklund, 2016). Moreover, iCCH hepatocytes collected at 36 hr after PHx displayed a reduction in basal and ATP-linked respiration (Figure 4J), suggesting that iCCH hepatocytes are not generating ATP efficiently

from mitochondrial respiration. We also measured the mitochondrial membrane potential by tetramethylrhodamine ethyl ester (TMRE) staining of hepatocytes. We first standardized conditions to label hepatocytes (see Figures S4G–S4I). Then, we quantified TMRE fluorescence, which indicated that before liver resection there was no significant reduction in TMRE accumulation in mitochondria of iCCH hepatocytes compared to iWT (Figures 4K and 4L). In contrast, at 36 hr after liver resection, iCCH hepatocytes displayed a substantially reduced TMRE signal (Figures 4M and 4N). These results confirmed that during liver regeneration, iCCH hepatocytes display reduced mitochondrial metabolism.

Transcriptomic and Metabolomic Integration Uncovers that Liver Regeneration by CCH Leads to Increased Amino Acid Metabolism

In order to understand the global changes of metabolic pathways involved and to gain functional insights into the changes of metabolism in the regenerating liver, we performed untargeted metabolomic analysis using QTOF mass spectrometry. Using integrative analysis (for a full description of the bioinformatics analysis, please refer to STAR Methods), we mapped RNA-seq and QTOF data to common pathways (Kanehisa and Goto, 2000).

To understand which metabolic pathways may be compensating for reduction in oxidative metabolism, we performed three comparisons of the integrated data. Initially, we compared each dataset of the WT to before PHx (Table S1); we then did the same comparison for CCH samples. Finally, we compared WT and CCH before and at each time point during liver regeneration. Pathway analysis was performed, and maps were manually built to depict the majority of the changes observed in WT (Figures S5A–S5D) as well as in the CCH livers (Figures S5E–S5H; Table S2) to the corresponding "before PHx" control samples. We observed novel metabolic pathways upregulated in WT liver after PHx, such as amino sugar and nucleoside sugar metabolism, while glucagon metabolism and biosynthesis of amino acids were downregulated at all time points (Figures S5B and S5C). From the CCH time-point-to-before comparison, we observed that biosynthesis of amino acids was upregulated, while carbon metabolism was decreased (Figures S5F and S5G).

We then studied the changes observed in CCH liver samples when compared directly to WT liver samples. When we integrated RNA-seq and metabolomic data to common pathways, we observed an overlap of 12 pathways significantly changed simultaneously at *all* time points (Figure 5A and Table S3), suggesting processes specific for hypertrophy and/or *Cdk1* deletion. Specifically, we noticed that when compared to WT, CCH livers displayed downregulation of biosynthesis of secondary metabolites and carbohydrates but upregulation of alanine, aspartate, and glutamine metabolism (Figure 5B). We created maps with common changes in mRNA levels and metabolites to depict the overall changes in the metabolomic landscape of the regenerating liver (Figure 5C). Overall, we detected decreases in amino acid metabolism including fumarylacetoacetate hydrolase *(Fah)* and argininosuccinate synthase 1 *(Ass1)*, the loss of which had been shown to display a similar phenotype to our mice (Wang et al., 2003). In addition, there was an increase in signaling pathways including *CREB*, *Jun*, *ERK*, *AKT*, and *AMPK* with the latter two being time point specific.

To validate these general findings, we performed targeted metabolic LC/MS analysis (Figures 5D–5I). We observed a slight reduction of carbon metabolism derivatives of carbohydrates such as hexoses and phosphoenolpyruvate in CCH (Figures 5D and 5E). There were no major changes in ATP and GMP levels (Figures 5F and 5G), suggesting that energy production was still maintained at sustainable levels in both WT and CCH. This could be explained as a compensatory effect of other pathways since it is well established that under normal conditions, reduced oxidative metabolism may be rescued by other pathways (Locasale and Cantley, 2011). To investigate whether this is true, we determined the levels of malate and aspartate, which were comparable in WT and CCH, suggesting that other sources are more likely to contribute as a compensatory pathway (Figures 5H and 5I). At the same time, we validated the mRNA expression of several enzymes in the carbohydrate (Figures 5J–5M) and amino acid (Figures 5N and 5O) metabolism by qPCR. We observed that *G6Pase* levels were relatively constant in WT, whereas in CCH there were peaks at 36 hr and 168 hr, indicating possible fluctuations during liver regeneration (Figure 5J). Both *Pepck* and *Pfkl* seemed to peak around 8 hr with a subsequent decrease (Figures 5K and 5L); while *Pklr*, a liver isoform of pyruvate kinase, was significantly reduced at 8–96 hr (Figure 5M), suggesting that carbohydrate metabolism may be reduced. Genes encoding for the mitochondrial ALT *(Gpt2)* and aspartate transaminase (AST) (*Got1*) peaked at 8 hr with a subsequent decrease during regeneration in both WT and CCH (Figures 5N and 5O), suggesting that when the expression of enzymes in carbohydrate metabolism is reduced, there is a concomitant increase in expression of enzymes involved in transamination.

In summary, the results from these experiments suggest that when cell division is reduced in hepatocytes, reduced hepatic NADH correlates with increases in amino acid metabolism. Although this is indirect evidence, taken together, these results may imply that only mitochondrial NADH-generating sources may be affected, since redox coenzymes may originate from other sources such as the malate-aspartate mitochondrial shuttle. Finally, increases in expression in mitochondrial ALT (*Gpt2*) suggest that pyruvate transamination could play an important role in this metabolic remodeling.

Liver Regeneration by Compensatory Cellular Hypertrophy Leads to Remodeling of the Pyruvate Flux

Bioinformatic integration of metabolomic and transcriptomic data suggested that both biological oxidations and carbohydrate metabolism were decreased during liver regeneration by CCH. However, we observed an increase in alanine and glutamine pathways, suggesting a shift from carbohydrate to glutamine utilization, similar to reductive carboxylation observed in cancer cells with defective mitochondria (Mullen et al., 2011). We then measured the metabolic flux of key enzymes involved in the conversion of pyruvate to carbohydrates or amino acids during regeneration. To do so, we used *in vivo* metabolic flux quantification by hyperpolarized ^{13}C-pyruvate and functional magnetic resonance imaging (fMRI) (Lee et al., 2013). With this approach, we measured the metabolic flux of the AST and pyruvate

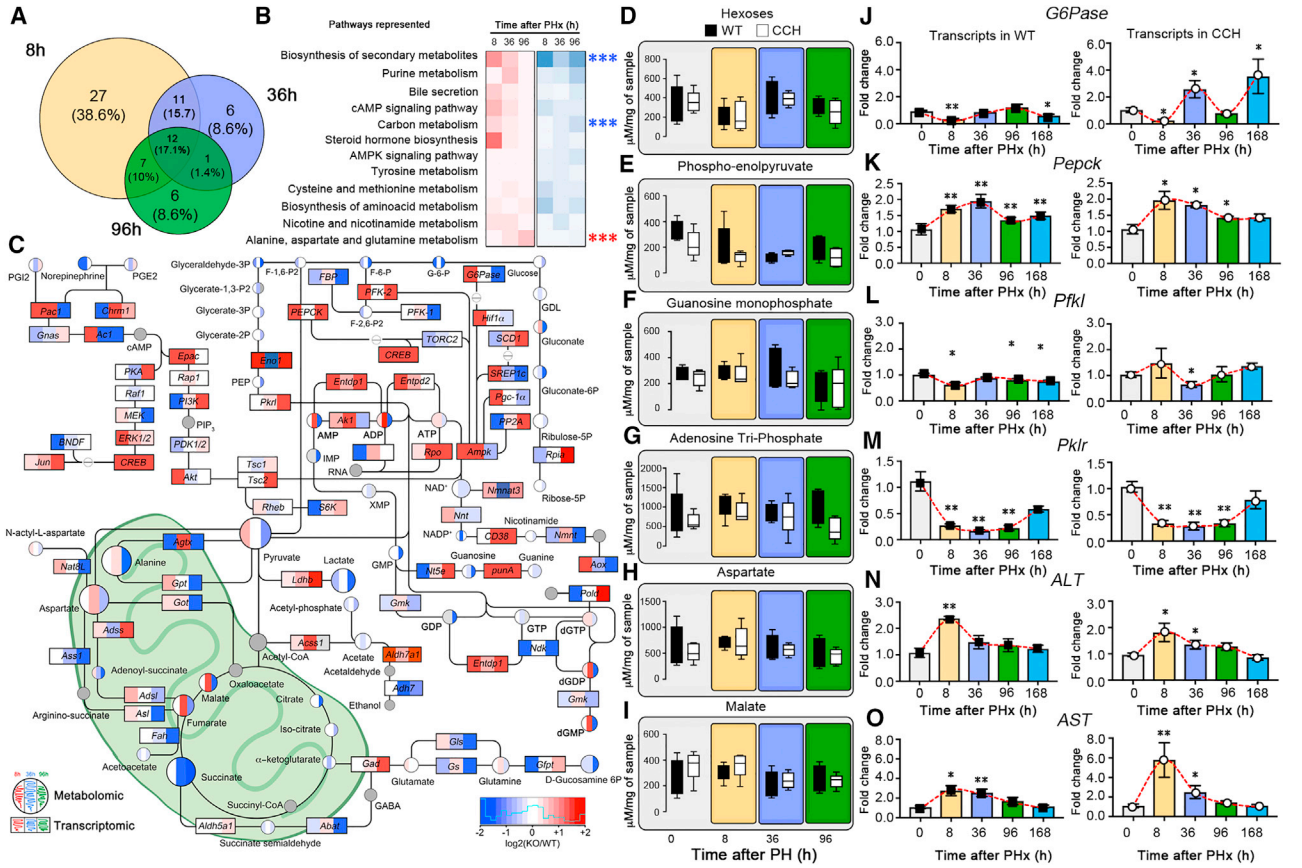

Figure 5. Integration of Metabolomic and Transcriptomic Analysis Suggests Metabolic Remodeling during Liver Regeneration by CCH

(A) Venn diagram with the number of pathways from data integration of metabolomic and transcriptomic data obtained from WT and CCH regenerating livers.

(B) Heatmaps of 12 pathways common to all of the time points during liver regeneration in CCH compared to WT liver.

(C) Map of the integration of metabolomic and transcriptomic analysis. Circles represent metabolites detected by QTOF, while rectangles represent transcripts from RNA sequencing data. Each circle and rectangle is divided into three sections, representing each of the time points during liver regeneration, 8 hr, 36 hr, and 96 hr after liver resection.

(D–I) Levels of metabolites in µM was measured by quantitative LC/MS.

(J–O) mRNA expression of *G6Pase*, *Pepck*, *Pfkl*, *Pklr*, *ALT*, and *AST* was determined by qPCR during liver regeneration (mean and SEM).

ALT, alanine transaminase; AST, aspartate aminotransferase.

carboxylase+pyruvate dehydrogenase (PC+PDH) as well as lactate dehydrogenase (LDH) and ALT, which will convert glucose-derived pyruvate into lactate and alanine, respectively (Figure 6A). We did not detect major differences for AST and PC+PDH under any condition (see Figures S7A–S7D), suggesting that acetyl-CoA and aspartate levels were likely not affected. Before liver resection, the metabolic flux of LDH and ALT was only slightly increased in CCH compared to WT littermates (Figures 6B and 6C), indicating comparable metabolism. In contrast, at 36 hr after PHx, we observed a significant increase in the liver-specific ALT metabolic flux (Figure 6E) but not in LDH (Figure 6D) in CCH animals when compared to WT littermates. This confirmed our previous assumptions that during tissue regeneration by CCH, carbohydrate metabolites (pyruvate) may be directed toward alanine instead of lactate production.

In order to confirm our results at the substrate and product level, we used quantitative LC/MS spectrometry to measure essential metabolites involved in the bi-directional conversion of pyruvate to alanine and lactate at different time points during liver regeneration. In WT liver, the levels of α-ketoglutarate, lactate, glutamine, and glutamate were fairly constant during the time course of liver regeneration, but pyruvate and alanine decreased slightly at later time points (Figure 6F). In CCH liver, pyruvate, lactate, and glutamine were constant, but there was a significant increase of alanine, α-ketoglutarate, and glutamine during regeneration. These data further supported a central role of alanine during liver regeneration by CCH. Besides alanine, we also observed that glutamate and α-ketoglutarate were increased in CCH liver during regeneration, suggesting increased use of glutamine for anabolic pathways, when mitochondria are not working efficiently (Locasale and Cantley, 2011). To confirm this, we measured a surrogate marker of amino acid metabolism, blood urea nitrogen (BUN). Increased levels of BUN in circulatory blood have been previously associated with protein catabolism, while reduced blood BUN with anabolism (Lamers et al., 2011). We observed a reduction in BUN in CCH mice compared to WT at all time points studied except 168 hr (Figure 6H), suggesting that in CCH livers, mitochondrial oxidation is reduced with a

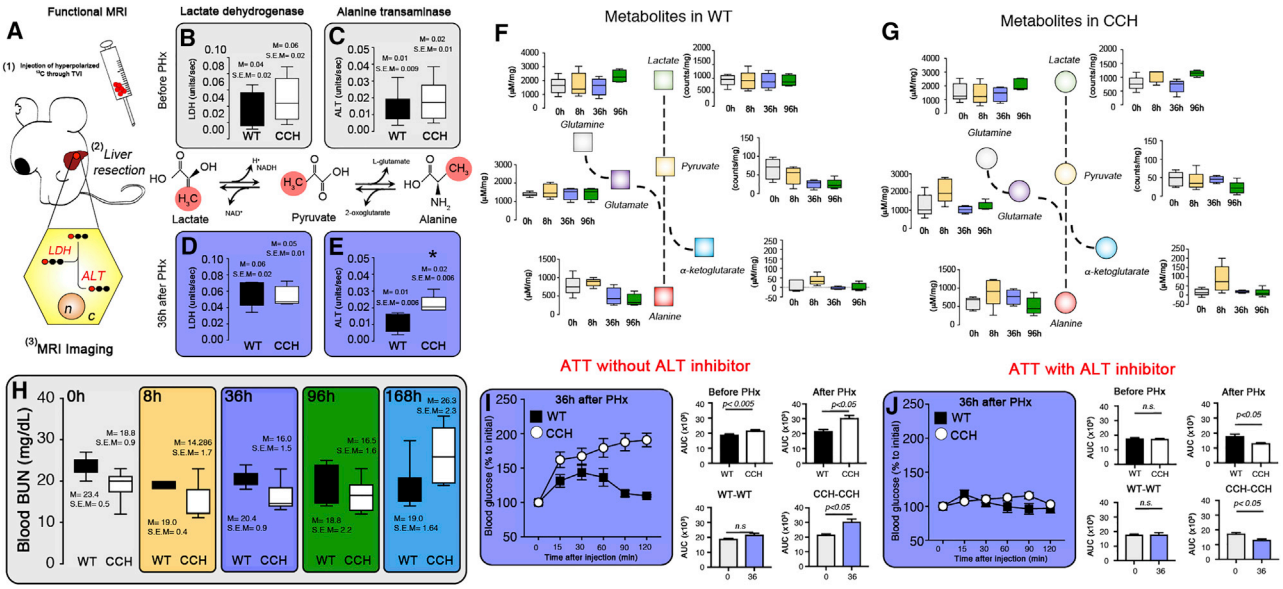

Figure 6. Increases in Alanine Metabolism during Liver Regeneration in CCH Liver Fuels the Production of α-ketoglutarate and Glucose

(A) Schematic representation of functional MRI analysis using hyperpolarized ^{13}C pyruvate.

(B–G) Measurements of metabolic fluxes of lactate dehydrogenase and alanine transaminase before (B and C) and at 36 hr after (D and E) PHx. Concentration of metabolites in μM per mg of liver tissue for alanine, α-ketoglutarate, glutamine, and glutamate, as well as counts of metabolites per milligram of liver tissue for lactate and pyruvate in WT (F) and CCH (G) livers at 0, 8, 36, and 96 hr after liver resection.

(H) Blood urea nitrogen (BUN) quantified from peripheral blood of WT and CCH mice at 0 hr, 8 hr, 36 hr, 96 hr, and 168 hr after PHx.

(I and J) Alanine tolerance test in WT and CCH livers at 36 hr after PHx in the absence (I) or presence (J) of the transaminases inhibitor aminooxyacetic acid hemihydrochloride (AOA) is shown with corresponding bar graphs for analysis of the area under the curve (AUC). Data are represented as the mean value, and error bars display the standard error of the mean.

LDH, lactate dehydrogenase; BUN, blood urea nitrogen; ATT, alanine tolerance test; AUC, area under the curve.

concomitant increase in ALT activity and alanine production to maintain anabolic pathways for liver regeneration.

Finally, we addressed potential physiological consequences of increased ALT activity during liver regeneration. One of the main fates of alanine in the liver is to support gluconeogenesis (Rui, 2014). Therefore, we tested whether increased ALT activity affects glucose levels when mitochondrial metabolism is impaired. We performed alanine tolerance tests (ATTs), where we injected a bolus of alanine in previously fasted mice (16 hr) and measured glucose levels from blood at different time points after the intraperitoneal (IP) injections. In WT mice, alanine injections had minor effects on glucose levels with an insignificant increase after 36 hr post PHx that returned to normal within less than 90 min. In CCH liver before liver resection, the glucose levels were comparable to WT (Figure S7N). Interestingly, 36 hr after liver resection, we observed a significant increase in blood glucose levels in CCH compared to WT mice after alanine injection, reaching 2-fold levels 120 min after injection (Figure 6I).

In order to further validate that this effect was caused by the increased activity of ALT, we blocked ALT activity using the transaminase inhibitor aminooxyacetic acid hemihydrochloride (AOA) (Beuster et al., 2011; Weinberg et al., 2010). We first tested the concentration of AOA required to reduce activity of ALT without affecting the vital signs of mice (see STAR Methods; Figures S7E–S7M). Before PHx, as a response to AOA injection, glucose levels increased by 50% in both WT and CCH animals (Figure S7J), but it had no effect on normalized glucose levels (Figure S7O) or when PBS was injected (Figures S7P and S7Q). We then injected AOA for 5 days and did liver resection in CCH and WT littermates, followed by the alanine tolerance test at 36 hr after PHx. In both CCH and WT mice, glucose levels remained unchanged (Figure 6J), suggesting that alanine increases blood glucose levels only in the presence of active ALT.

DISCUSSION

The importance of understanding the role of metabolism and cell division during liver regeneration is based on the fact that malfunction of these processes usually leads to liver failure (Huang and Rudnick, 2014). Other than the clinical relevance of studying liver regeneration, it is also a useful model to understand how cell cycle regulation integrates with pathways including transcription, signal transduction, metabolism, and tissue regeneration *in vivo*. To understand the mechanistic relationship between cell division and metabolism, we studied the metabolic regulation in two models of liver regeneration after PHx, namely regeneration by compensatory cellular hyperplasia (normal liver regeneration) and regeneration by CCH. We discovered that in our CCH mouse model of liver regeneration, tissue repair takes place despite a significant downregulation of oxidative pathways and reduction of mitochondrial respiration, which results in metabolic remodeling involving increased metabolic flux through ALT.

Since there are no *in vitro* models to study metabolic remodeling of the regenerating liver, we used a combination of "omics"

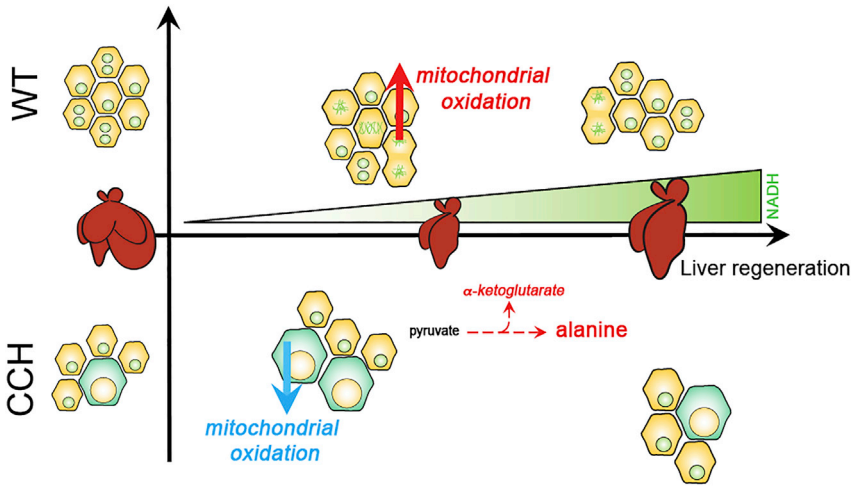

Figure 7. Model of Metabolic Changes during Liver Regeneration by Compensatory Cellular Hypertrophy

Normal liver regeneration by compensatory cellular hyperplasia (WT; growth involving cell division) is associated with time-dependent increases of redox equivalents, particularly NADH, to maintain appropriate redox balance. However, when hepatocyte division is blocked, biological oxidation is reduced with a concomitant decrease of NADH levels, which is linked to diminished mitochondrial functions. To complete regeneration, CCH hepatocytes remodel their metabolism, resulting in increased production of alanine and α-ketoglutarate from pyruvate to recover organ size by compensatory cellular hypertrophy.

data with *in vivo* intravital imaging of redox equivalents and metabolic fluxes (Figures 2, 3, and 6). Initially, we developed a protocol to image regenerating livers using two-photon fluorescence microscopy (TPFM) (Figure S2), which was a useful tool to grasp the dynamic changes of two essential cofactors involved in oxidative pathways, NADH and FAD. The ratio of these cofactors known as the redox ratio is a robust indicator of the metabolic status of a cell (Georgakoudi and Quinn, 2012). It has been observed that increases in total NADH and therefore a reduction in the redox ratio follow division of cancer cells (Skala et al., 2007), differentiation of stem cells (Quinn et al., 2013), as well as in metastatic events (Ritsma et al., 2012). Moreover, in terminally differentiated cells, redox equivalents (NADH and FAD) are important effectors of biological oxidation (Locasale and Cantley, 2011), which implies that cell division and differentiation rely substantially on NADH, in agreement with what was observed in WT mice during regeneration (Figures 2B and 2E). In CCH livers, cells are not able to divide, and therefore total NADH is reduced (Figure 3J). Although these data agree with transcriptomic analysis (Figure 3D), it remains unclear whether the lower levels of NADH in our CCH model are a cause or a consequence of impaired cell division. Future efforts should be made to understand the direction of this relationship.

Progression through the cell cycle, especially during the growth phase and S-phase, requires a significant amount of metabolites (nucleotides) as well as activation of biosynthetic pathways to support DNA synthesis and cellular growth (Locasale and Cantley, 2011). Therefore, we expected a metabolic remodeling at this particular time point when oxidative pathways are reduced in our mutant mice. Since *Cdk1* is an essential gene needed for cell division, it is expected that it may have new functions, such as controlling metabolic pathways. In fact, there were earlier indications that Cdk1 interacts with glycolysis (Yalcin et al., 2014; Yuan et al., 2008) and mitochondrial metabolism during cell division and DNA repair (Liu et al., 2015; Qin et al., 2015; Wang et al., 2014). Yet, these connections have not been shown *in vivo* due to technical limitations. Here, we provide additional evidence that the cell cycle interacts with metabolic pathways either directly or indirectly through Cdk1. We also recognize that there may be additional effects in our mouse model, which could influence the results obtained. However, the strength of our mouse model is that failure in cell division and consecutive changes in cell size have been associated with a wide range of liver pathology (Gentric et al., 2015; Ogrodnik et al., 2017).

To study metabolic remodeling, we used a second *in vivo* approach. Analysis of ^{13}C-pyruvate flux has been developed as a useful methodology to measure *in vivo* changes in the metabolic and energetic profile of cells (DeBerardinis et al., 2007), which has direct potential clinical implications. However, metabolic remodeling of pyruvate flux has not been studied before during liver regeneration. We observed an increase in ALT metabolic flux in CCH livers (Figure 6). A similar effect was previously observed during the pre-tumorigenic stage of hepatocellular carcinoma (HCC) (Hu et al., 2011), which is characterized by increases in hepatocyte size. This further supports the idea that increases in the flux of ALT may be a key feature in hepatocyte hypertrophy. At the same time, a similar metabolic remodeling was observed upon impaired pyruvate import to the mitochondria (Gray et al., 2015; McCommis et al., 2015), suggesting that increasing the metabolic flux through ALT may compensate for pyruvate oxidation. Finally, clinical studies reported a positive correlation between transaminase levels and mitochondrial dysfunction after liver surgery (Alexandrino et al., 2016; Auger et al., 2015), further highlighting the significance of our discovery. The equilibrium of the ALT reaction is dependent on substrate and product levels, and thus metabolic flux through ALT can be bi-directional (Beuster et al., 2011; Smeitink et al., 2006), which is also evident from our ^{13}C-pyruvate flux analysis and ATT (Figure 6). Normally, alanine is produced in muscle and converted to pyruvate in the liver (Rui, 2014), but we do not believe this is what is happening in our knockout mice. Our data suggest that alanine is not a mere liver damage marker, but it plays a role in tissue repair beyond that of NAD^+/NADH redox balance. Although there are a lot of questions about the functions of alanine, under the conditions tested, ALT activity has an effect on blood glucose levels as observed upon inhibition of ALT by AOA (Figures 6I and 6J) because either alanine is able to support gluconeogenesis (Rui, 2014)

or reduce the need for glucose uptake in the liver (Beuster et al., 2011). Additional experiments are required to fully uncover the role of ALT in tissue repair as AOA may also inhibit other transaminases. Overall, these data suggest that alanine production is the preferred route for pyruvate in CCH livers. This is because pyruvate-derived acetyl-CoA may not efficiently enter the TCA cycle when mitochondria are dysfunctional, and if pyruvate would be converted to lactate, this would further increase the substantial NAD^+/NADH imbalance in CCH liver (Figure 3N). Finally, the added benefit of pyruvate to alanine conversion is that alanine can potentially be used as a future gluconeogenic substrate for organismal needs.

In summary, we used a combination of transcriptomic and metabolomic data analysis in combination with intravital functional imaging to describe the metabolic landscape of the regenerating liver (Figure 7). We uncovered metabolic remodeling activated by impaired mitochondrial function and reduced cellular oxidation, particularly when liver regenerates by cellular compensatory hypertrophy. Although we focused on the increase in ALT metabolic flux during this process, the fact that other metabolic changes may be contributing simultaneously should be taken into consideration. A direct clinical implication of our work is the possibility of modulating NADH levels using NAD^+ repletion to promote hepatocyte division after tissue damage or the modulation of alanine levels. Future research will further validate these metabolic changes in the clinical setting and help to develop novel clinical biomarkers for liver regeneration.

STAR★METHODS

Detailed methods are provided in the online version of this paper and include the following:

- KEY RESOURCES TABLE
- CONTACT FOR REAGENT AND RESOURCE SHARING
- EXPERIMENTAL MODEL AND SUBJECT DETAILS
  - Animals
- METHOD DETAILS
  - Genetic Model, and Liver and Blood Sampling
  - 70% Partial Hepatectomy
  - Transcriptomic Analysis
  - QTOF Metabolomic and LC/MS Analysis
  - Bioinformatic Analysis
  - Intravital Imaging Using Two-Photon Microscopy Imaging
  - Hepatocyte Isolation, Culture, and Immunocytochemistry
  - Analysis of Hepatocytes Respiration
  - ^{13}C-Pyruvate Metabolic Flux Analysis
  - RNA Isolation and RT-qPCR
  - Western Blotting
  - AOA and Alanine Tolerance Test
  - Statistics

SUPPLEMENTAL INFORMATION

Supplemental Information includes seven figures and three tables and can be found with this article online at https://doi.org/10.1016/j.devcel.2018.09.020.

ACKNOWLEDGMENTS

We would like to thank all members of the Kaldis lab for discussion and support; Joanna Niska-Blakie for comments on the manuscript; Uwe Sauer (ETH Zürich) for support and advice; and the vets and technicians from Biological Resource Centre (BRC-A*STAR Singapore) for veterinary assistance. Special thanks go to Tan Qing Hui, Shiela Fransisco Margallo, and Pangalingan Christie Chrisma Domingo. We acknowledge the technical expertise provided by the Advanced Molecular Pathology Laboratory at IMCB.

This work is supported by the Biomedical Research Council, Agency for Science, Technology and Research (A*STAR) to P.K., H.Y., P.L., W.S., and H.C.; SINGA (Singapore InterNational Graduate Award) to M.J.C.; the Institute of Bioengineering and Nanotechnology, A*STAR (Project Number 1334i00051 to H.Y.); NMRC (R-185-000-294-511 to H.Y.); SMART BioSyM and Mechanobiology Institute of Singapore (R-714-001-003-271 to H.Y.); and the Biomedical Research Council – Joint Council Office Grant (1231AFG031 to P.K. and P.L.).

AUTHOR CONTRIBUTIONS

Conceptualization, M.J.C., M.B., and P.K.; Methodology, M.J.C., N.V.H., H.W.L.K., J.J.F., X.Q.T., and P.Y.T.; Software, H.W.L.K. and H.C.; Formal Analysis, M.J.C. and H.W.L.K.; Investigation, M.J.C., N.V.H., X.Q.T., P.L., J.J.F., S.Z.A.T., B.E.C., M.R.D., and T.F.; Resources, M.J.C., H.W.L.K., H.C., P.L., J.J.F., W.S., H.Y., T.F., M.B., and P.K.; Writing – Original Draft, M.J.C., N.V.H., M.B., and P.K.; Writing – Review & Editing, M.J.C., M.B., and P.K.; Visualization, M.J.C. and H.W.L.K.; Supervision, P.K., M.B., H.C., P.L., H.Y., and T.F.; Project Administration, M.J.C., P.K., and M.B.; Funding Acquisition, P.K., M.B., and P.L.

DECLARATION OF INTERESTS

H.Y. declares that he is the founding scientist with minority share in HistoIndex Pte Ltd (www.histoindex.com), Pishon Biomedical Co. Ltd (www.bbbmd.com), and Invitrocue (Pte) Ltd (www.invitrocue.com), which have business interest in the area of imaging liver diseases, selling products, or providing hepatotoxicity testing services but have no conflict of interest with the work presented in this manuscript. All other authors declare no competing interests.

Received: November 3, 2017
Revised: May 13, 2018
Accepted: September 21, 2018
Published: October 18, 2018

REFERENCES

Alexandrino, H., Varela, A.T., Teodoro, J.S., Martins, M.A., Rolo, A.P., Tralhão, J.G., Palmeira, C.M., and Castro E Sousa, F. (2016). Mitochondrial bioenergetics and posthepatectomy liver dysfunction. Eur. J. Clin. Invest. *46*, 627–635.

Ashburner, M., Ball, C.A., Blake, J.A., Botstein, D., Butler, H., Cherry, V., Davis, A.P., Dolinski, K., Dwight, S.S., Eppig, J.T., et al. (2000). Gene ontology: tool for the unification of biology. The Gene Ontology Consortium. Nat. Genet. *25*, 25–29.

Auger, C., Alhasawi, A., Contavadoo, M., and Appanna, V.D. (2015). Dysfunctional mitochondrial bioenergetics and the pathogenesis of hepatic disorders. Front. Cell Dev. Biol. *3*, 40.

Beuster, G., Zarse, K., Kaleta, C., Thierbach, R., Kiehntopf, M., Steinberg, P., Schuster, S., and Ristow, M. (2011). Inhibition of alanine aminotransferase in silico and in vivo promotes mitochondrial metabolism to impair malignant growth. J. Biol. Chem. *286*, 22323–22330.

Buescher, J.M., Moco, S., Sauer, U., and Zamboni, N. (2010). Ultrahigh performance liquid chromatography-tandem mass spectrometry method for fast and robust quantification of anionic and aromatic metabolites. Anal. Chem. *82*, 4403–4412.

DeAngelis, R.A., Markiewski, M.M., Taub, R., and Lambris, J.D. (2005). A high-fat diet impairs liver regeneration in C57BL/6 mice through

overexpression of the NF-kappaB inhibitor, IkappaBalpha. Hepatology *42*, 1148–1157.

DeBerardinis, R.J., Mancuso, A., Daikhin, E., Nissim, I., Yudkoff, M., Wehrli, S., and Thompson, C.B. (2007). Beyond aerobic glycolysis: transformed cells can engage in glutamine metabolism that exceeds the requirement for protein and nucleotide synthesis. Proc. Natl. Acad. Sci. USA *104*, 19345–19350.

Diril, M.K., Ratnacaram, C.K., Padmakumar, V.C., Du, T., Wasser, M., Coppola, V., Tessarollo, L., and Kaldis, P. (2012). Cyclin-dependent kinase 1 (Cdk1) is essential for cell division and suppression of DNA re-replication but not for liver regeneration. Proc. Natl. Acad. Sci. USA *109*, 3826–3831.

Dragin, N., Smani, M., Arnaud-Dabernat, S., Dubost, C., Moranvillier, I., Costet, P., Daniel, J.Y., and Peuchant, E. (2006). Acute oxidative stress is associated with cell proliferation in the mouse liver. FEBS Lett. *580*, 3845–3852.

Eguchi, A., Wree, A., and Feldstein, A.E. (2014). Biomarkers of liver cell death. J. Hepatol. *60*, 1063–1074.

el-Deiry, W.S., Tokino, T., Velculescu, V.E., Levy, D.B., Parsons, R., Trent, J.M., Lin, D., Mercer, W.E., Kinzler, K.W., and Vogelstein, B. (1993). WAF1, a potential mediator of p53 tumor suppression. Cell *75*, 817–825.

Fausto, N., Campbell, J.S., and Riehle, K.J. (2006). Liver regeneration. Hepatology *43*, S45–S53.

Feher, J.J. (2012). Quantitative Human Physiology: An Introduction (Academic Press), pp. 180–190.

Forbes, S.J., and Newsome, P.N. (2016). Liver regeneration - mechanisms and models to clinical application. Nat. Rev. Gastroenterol. Hepatol. *13*, 473–485.

Fuhrer, T., Heer, D., Begemann, B., and Zamboni, N. (2011). High-throughput, accurate mass metabolome profiling of cellular extracts by flow injection-time-of-flight mass spectrometry. Anal. Chem. *83*, 7074–7080.

Gentric, G., Maillet, V., Paradis, V., Couton, D., L'Hermitte, A., Panasyuk, G., Fromenty, B., Celton-Morizur, S., and Desdouets, C. (2015). Oxidative stress promotes pathologic polyploidization in nonalcoholic fatty liver disease. J. Clin. Invest. *125*, 981–992.

Georgakoudi, I., and Quinn, K.P. (2012). Optical imaging using endogenous contrast to assess metabolic state. Annu. Rev. Biomed. Eng. *14*, 351–367.

Gray, L.R., Sultana, M.R., Rauckhorst, A.J., Oonthonpan, L., Tompkins, S.C., Sharma, A., Fu, X., Miao, R., Pewa, A.D., Brown, K.S., et al. (2015). Hepatic mitochondrial pyruvate carrier 1 is required for efficient regulation of gluconeogenesis and whole-body glucose homeostasis. Cell Metab. *22*, 669–681.

Guguen-Guillouzo, C. (2002). Isolation and culture of animal and human hepatocytes. In Culture of Epithelial Cells, R. Freshney and M. Frshney, eds. (Wiley-Liss, Inc.), pp. 337–379.

Haga, S., Ogawa, W., Inoue, H., Terui, K., Ogino, T., Igarashi, R., Takeda, K., Akira, S., Enosawa, S., Furukawa, H., et al. (2005). Compensatory recovery of liver mass by Akt-mediated hepatocellular hypertrophy in liver-specific STAT3-deficient mice. J. Hepatol. *43*, 799–807.

Hu, S., Balakrishnan, A., Bok, R.A., Anderton, B., Larson, P.E., Nelson, S.J., Kurhanewicz, J., Vigneron, D.B., and Goga, A. (2011). 13C-pyruvate imaging reveals alterations in glycolysis that precede c-Myc-induced tumor formation and regression. Cell Metab. *14*, 131–142.

Huang, J., and Rudnick, D.A. (2014). Elucidating the metabolic regulation of liver regeneration. Am. J. Pathol. *184*, 309–321.

Kamburov, A., Stelzl, U., Lehrach, H., and Herwig, R. (2013). The ConsensusPathDB interaction database: 2013 update. Nucleic Acids Res. *41*, D793–D800.

Kanehisa, M., and Goto, S. (2000). KEGG: Kyoto encyclopedia of genes and genomes. Nucleic Acids Res. *28*, 27–30.

Koh, H.W., Swa, H.L., Fermin, D., Ler, S.G., Gunaratne, J., and Choi, H. (2015). EBprot: statistical analysis of labeling-based quantitative proteomics data. Proteomics *15*, 2580–2591.

Lamers, W., Hakvoort, T., and Köhler, E. (2011). Hepatic protein metabolism. In Molecular Pathology of Liver Diseases, S. Mong, ed. (Springer Science), pp. 125–132.

Lee, P., Leong, W., Tan, T., Lim, M., Han, W., and Radda, G.K. (2013). In vivo hyperpolarized carbon-13 magnetic resonance spectroscopy reveals increased pyruvate carboxylase flux in an insulin-resistant mouse model. Hepatology *57*, 515–524.

Liu, R., Fan, M., Candas, D., Qin, L., Zhang, X., Eldridge, A., Zou, J.X., Zhang, T., Juma, S., Jin, C., et al. (2015). CDK1-mediated SIRT3 activation enhances mitochondrial function and tumor radioresistance. Mol. Cancer Ther. *14*, 2090–2102.

Livak, K.J., and Schmittgen, T.D. (2001). Analysis of relative gene expression data using real-time quantitative PCR and the 2(-ΔΔCt) Method. Methods *25*, 402–408.

Locasale, J.W., and Cantley, L.C. (2011). Metabolic flux and the regulation of mammalian cell growth. Cell Metab. *14*, 443–451.

McCommis, K.S., Chen, Z., Fu, X., McDonald, W.G., Colca, J.R., Kletzien, R.F., Burgess, S.C., and Finck, B.N. (2015). Loss of mitochondrial pyruvate carrier 2 in the liver leads to defects in gluconeogenesis and compensation via pyruvate-alanine cycling. Cell Metab. *22*, 682–694.

Miettinen, T.P., Pessa, H.K., Caldez, M.J., Fuhrer, T., Diril, M.K., Sauer, U., Kaldis, P., and Björklund, M. (2014). Identification of transcriptional and metabolic programs related to mammalian cell size. Curr. Biol. *24*, 598–608.

Miettinen, T.P., and Björklund, M. (2016). Cellular allometry of mitochondrial functionality establishes the optimal cell size. Dev. Cell *39*, 370–382.

Minamishima, Y.A., Nakayama, K., and Nakayama, K. (2002). Recovery of liver mass without proliferation of hepatocytes after partial hepatectomy in Skp2-deficient mice. Cancer Res. *62*, 995–999.

Mitchell, C., and Willenbring, H. (2008). A reproducible and well-tolerated method for 2/3 partial hepatectomy in mice. Nat. Protoc. *3*, 1167–1170.

Miyaoka, Y., Ebato, K., Kato, H., Arakawa, S., Shimizu, S., and Miyajima, A. (2012). Hypertrophy and unconventional cell division of hepatocytes underlie liver regeneration. Curr. Biol. *22*, 1166–1175.

Mullen, A.R., Wheaton, W.W., Jin, E.S., Chen, P.H., Sullivan, L.B., Cheng, T., Yang, Y., Linehan, W.M., Chandel, N.S., and DeBerardinis, R.J. (2011). Reductive carboxylation supports growth in tumour cells with defective mitochondria. Nature *481*, 385–388.

Ogrodnik, M., Miwa, S., Tchkonia, T., Tiniakos, D., Wilson, C.L., Lahat, A., Day, C.P., Burt, A., Palmer, A., Anstee, Q.M., et al. (2017). Cellular senescence drives age-dependent hepatic steatosis. Nat. Commun. *8*, 15691.

Qin, L., Fan, M., Candas, D., Jiang, G., Papadopoulos, S., Tian, L., Woloschak, G., Grdina, D.J., and Li, J.J. (2015). CDK1 enhances mitochondrial bioenergetics for radiation-induced DNA repair. Cell Rep. *13*, 2056–2063.

Quinn, K.P., Sridharan, G.V., Hayden, R.S., Kaplan, D.L., Lee, K., and Georgakoudi, I. (2013). Quantitative metabolic imaging using endogenous fluorescence to detect stem cell differentiation. Sci. Rep. *3*, 3432.

Richardson, M.M., Jonsson, J.R., Powell, E.E., Brunt, E.M., Neuschwander-Tetri, B.A., Bhathal, P.S., Dixon, J.B., Weltman, M.D., Tilg, H., Moschen, A.R., et al. (2007). Progressive fibrosis in nonalcoholic steatohepatitis: association with altered regeneration and a ductular reaction. Gastroenterology *133*, 80–90.

Ritsma, L., Steller, E.J., Beerling, E., Loomans, C.J., Zomer, A., Gerlach, C., Vrisekoop, N., Seinstra, D., van Gurp, L., Schäfer, R., et al. (2012). Intravital microscopy through an abdominal imaging window reveals a pre-micrometastasis stage during liver metastasis. Sci. Transl. Med. *4*, 158ra145.

Ritsma, L., Steller, E.J., Ellenbroek, S.I., Kranenburg, O., Borel Rinkes, I.H., and van Rheenen, J. (2013). Surgical implantation of an abdominal imaging window for intravital microscopy. Nat. Protoc. *8*, 583–594.

Rui, L. (2014). Energy metabolism in the liver. Compr. Physiol. *4*, 177–197.

Rutter, J., Winge, D.R., and Schiffman, J.D. (2010). Succinate dehydrogenase - assembly, regulation and role in human disease. Mitochondrion *10*, 393–401.

Santamaría, D., Barrière, C., Cerqueira, A., Hunt, S., Tardy, C., Newton, K., Cáceres, J.F., Dubus, P., Malumbres, M., and Barbacid, M. (2007). Cdk1 is sufficient to drive the mammalian cell cycle. Nature *448*, 811–815.

Skala, M.C., Riching, K.M., Gendron-Fitzpatrick, A., Eickhoff, J., Eliceiri, K.W., White, J.G., and Ramanujam, N. (2007). In vivo multiphoton microscopy of

NADH and FAD redox states, fluorescence lifetimes, and cellular morphology in precancerous epithelia. Proc. Natl. Acad. Sci. USA *104*, 19494–19499.

Smeitink, J.A., Zeviani, M., Turnbull, D.M., and Jacobs, H.T. (2006). Mitochondrial medicine: a metabolic perspective on the pathology of oxidative phosphorylation disorders. Cell Metab. *3*, 9–13.

Tamori, Y., and Deng, W.M. (2014). Compensatory cellular hypertrophy: the other strategy for tissue homeostasis. Trends Cell Biol. *24*, 230–237.

Tretter, L., Patocs, A., and Chinopoulos, C. (2016). Succinate, an intermediate in metabolism, signal transduction, ROS, hypoxia, and tumorigenesis. Biochim. Biophys. Acta *1857*, 1086–1101.

Vander Heiden, M.G., Cantley, L.C., and Thompson, C.B. (2009). Understanding the Warburg effect: the metabolic requirements of cell proliferation. Science *324*, 1029–1033.

Vendemiale, G., Guerrieri, F., Grattagliano, I., Didonna, D., Muolo, L., and Altomare, E. (1995). Mitochondrial oxidative phosphorylation and intracellular glutathione compartmentation during rat liver regeneration. Hepatology *21*, 1450–1454.

Veteläinen, R., van Vliet, A.K., and van Gulik, T.M. (2007). Severe steatosis increases hepatocellular injury and impairs liver regeneration in a rat model of partial hepatectomy. Ann. Surg. *245*, 44–50.

Wang, X., Willenbring, H., Akkari, Y., Torimaru, Y., Foster, M., Al-Dhalimy, M., Lagasse, E., Finegold, M., Olson, S., and Grompe, M. (2003). Cell fusion is the principal source of bone-marrow-derived hepatocytes. Nature *422*, 897–901.

Wang, Z., Fan, M., Candas, D., Zhang, T.Q., Qin, L., Eldridge, A., Wachsmann-Hogiu, S., Ahmed, K.M., Chromy, B.A., Nantajit, D., et al. (2014). Cyclin B1/Cdk1 coordinates mitochondrial respiration for cell-cycle G2/M progression. Dev. Cell *29*, 217–232.

Weinberg, F., Hamanaka, R., Wheaton, W.W., Weinberg, S., Joseph, J., Lopez, M., Kalyanaraman, B., Mutlu, G.M., Budinger, G.R., and Chandel, N.S. (2010). Mitochondrial metabolism and ROS generation are essential for Kras-mediated tumorigenicity. Proc. Natl. Acad. Sci. USA *107*, 8788–8793.

Yalcin, A., Clem, B.F., Imbert-Fernandez, Y., Ozcan, S.C., Peker, S., O'Neal, J., Klarer, A.C., Clem, A.L., Telang, S., and Chesney, J. (2014). 6-Phosphofructo-2-kinase (PFKFB3) promotes cell cycle progression and suppresses apoptosis via Cdk1-mediated phosphorylation of p27. Cell Death Dis. *5*, e1337.

Yuan, Z., Becker, E.B., Merlo, P., Yamada, T., DiBacco, S., Konishi, Y., Schaefer, E.M., and Bonni, A. (2008). Activation of FOXO1 by Cdk1 in cycling cells and postmitotic neurons. Science *319*, 1665–1668.

STAR★METHODS

KEY RESOURCES TABLE

REAGENT or RESOURCE	SOURCE	IDENTIFIER
Antibodies		
OXPHOS	Abcam	ab110413; RRID: AB_2629281
HSP90	BD	610418; RRID: AB_397798
Ki67	Abcam	ab15580; RRID: AB_443209
Chemicals, Peptides, and Recombinant Proteins		
Tamoxifen	Sigma-Aldrich	T5648-5G
Corn Oil	Sigma-Aldrich	C8267-500ML
Liberase blenzyme 3	Roche	1814176
Collagen Type III (rat tail)	Corning	354236
PBS	Thermo Fisher	70011044
C-13 pyruvate probe	Cambridge Isotope Laboratories	CLM-1082-PK
Phalloidin	Thermo Fisher	A12379
DAPI	Thermo Fisher	D1306
Sodium Pyruvate	Sigma-Aldrich	P2256
Alanine	Sigma-Aldrich	05160-1KG
O-(carboxymethyl)hydroxyalanine hemihydrochloride	Sigma-Aldrich	C13408-1G
Critical Commercial Assays		
Alanine Transaminase Activity Assay Kit	Abcam	ab105134
NADP/NADPH Assay Kit	Abcam	ab65349
NAD/NADH Assay Kit	Abcam	ab65348
TMRE Mitochondrial Membrane Potential Assay Kit	Abcam	ab113852
Chemistry Comprehensive Rotors	Abaxis	#500-0038-12
Cellular phenotyping assay	Agilent Technologies	Kit 103275-100
Seahorse XF Cell Mito Stress Test Kit	Agilent Technologies	Kit 103015-100
Experimental Models: Organisms/Strains		
Mus musculus: *Cdk1*$^{flox/flox}$	Diril et al. (2012)	N/A
Mus musculus: Albumin-cre	B6.Cg-Tg(Alb-Cre)21Mgn/J	N/A
Mus musculus: Albumin-creERT2	Albtm1(cre/ERT2)Mtz	N/A
Oligonucleotides		
Cdk1Set1Fw: AGCGAGGAAGAAGGAGTGCC	This paper	PKO2004
Cdk1Set1Rv: CATGAGCACATCCTGCAGGC	This paper	PKO2005
Cdk1Set2Fw: ACGAGGTAGTGACGCTGTGG	This paper	PKO2006
Cdk1Set2Rv: GCCCAGAGCTCTGAAGATCC	This paper	PKO2007
p21Set1Fw: CCTTGTCGCTGTCTTGCACT	This paper	PKO2308
p21Set1Rv: AATCTGTCAGGCTGGTCTGC	This paper	PKO2309
p21Set2Fw: CCAGACATTCAGAGCCACA	This paper	PKO2817
p21Set2Rv: CACGGGACCGAAGAGACAA	This paper	PKO2818
Nadsyn1Fw: TGACAAAGCAGAAAAGTGTG	This paper	PKO6449
Nadsyn1Rev: ACCAGATCCACTCTGGTATG	This paper	PKO6450
Nmpt1Fw: CTCATCCAAGAAGACAGAGG	This paper	PKO6451
Nmpt1Rv: AGGTTCTGCCATGATGATTC	This paper	PKO6452
Gpx3Fw: ATACTCCCCAGTCTCAAG	This paper	PKO6453
Gpx3Rv: GGAGTTCTTCAGGAAAGTGT	This paper	PKO6454
CatFw: TACACGCAAAAGGAGCAG	This paper	PKO6455
CatRv: AGTGACTGTGGAGAATCG	This paper	PKO6456

(*Continued on next page*)

Continued

REAGENT or RESOURCE	SOURCE	IDENTIFIER
Sod1Fw: TACACAAGGCTGTACCAGT	This paper	PKO6457
Sod1Rv: AACATGCCTCTCTTCATCC	This paper	PKO6458
G6PaseFw: CTCCGTGCCTATAATAAAGC	This paper	PKO6459
G6PaseRv: TCAAACACCGGAATCCAT	This paper	PKO6460
PepckFw: TGATCCTGGGCATAACTAAC	This paper	PKO6461
PepckRv: CCTTGGGCATCAAACTTC	This paper	PKO6462
PfklFw: GTGAAGGATCTGGTGGTT	This paper	PKO6463
PfklRv: ACCCATCTTGCTACTCAG	This paper	PKO6464
PklrFw: TGAAGGCGTTGAAGAAGTT	This paper	PKO6465
PklrRv: CAGCGTCCAATCATCATC	This paper	PKO6466
Gpt2set1Fw: CAGCCAATCACCTTCCTC	This paper	PKO3880
Gpt2set1Rv: CTGTAAGATCCCAAGCTGT	This paper	PKO3881
Gpt2set2Fw: AGCAATTCAGCAGGGAAA	This paper	PKO3882
Gpt2Set2Rv: CTTGGCAGGGATGAGAAT	This paper	PKO3883
Gotset1Fw: TCCATCAGTCTTTGCCCA	This paper	PKO3868
Gotset1Rv: GCAATCTTCTGTTCGACC	This paper	PKO3869
Gotset2Fw: CCAACCTGGGAGAACCATA	This paper	PKO3870
Gotset2Rv: GGCTGAGTCAAAGAAGGG	This paper	PKO3871
eE2F1set1Fw: CACTTACCATCCCCCGTCAC	This paper	PKO3215
eE2F1set1Rv: CTTTGGGGTCGCAGCTCTTA	This paper	PKO3216
cycloAFw: CCTTGGGCCGCGTCTCCTT	This paper	PKO2002
cycloARv: CACCCTGGCACATGAATCCTG	This paper	PKO2003
Genotyping Cdk1Fw1: TTTGTCAAGAAATGCAGCAGGACAC	This paper	PKO0844
Genotyping Cdk1Rv1: GCTCACATGTTCCTGAATGGTGGA	This paper	PKO1158
Genotyping Cdk1Rv1: GCGGTGGTTTAAACCCATAATCCCGGCAC	This paper	PKO1006b
GenotypingAlbumin-creFw1: GGACAAAGTCTTGTGCATGG	This paper	PKO2656
GenotypingAlbumin-creRv1: CCAGGCTAAGTGCCTTCTCTACA	This paper	PKO2657
GenotypingAlbumin-creERT2Fw1: GGAACCCAAACTGATGACCA	This paper	PKO2653
GenotypingAlbumin-creERT2Rv1: TTAAACAAGCAAAACCAAAT	This paper	PKO2654
Cdk1E1Fw: GAGATCCTGGACTGTGTGAC	This paper	PKO5059
Cdk1E1Rv: GAGAAACACCCAGACAAAAG	This paper	PKO5060
Cdk1E3Fw: TTAGCAGTTATGCTGTTGGA	This paper	PKO5061
Cdk1E3Rv: TGGAGTCCAGGTACTTCTTG	This paper	PKO5062
Software and Algorithms		
Prism 7 for Mac OS X	GraphPad Software, Inc.	N/A
ImageJ	Public domain	N/A
XF Analyzer	Agilent, Public domain	N/A
TopHat	https://ccb.jhu.edu/software/tophat/index.shtml	N/A
CuffLinks	http://cole-trapnell-lab.github.io/cufflinks/	N/A
R	http://cran.r-project.org	N/A
EBprot	https://github.com/cssblab/EBprot	N/A
Other		
Microvette® 200, Li Hep, conical bottom	Kent Scientific Corp	MCVT200-LiHEP
9 mm EZ clip applier	Braintree scientific INC	EZC APL
9 mm EX clip remover	Braintree scientific INC	EZC RMV
Staples	Braintree scientific INC	EZC 2PK
Silk, braided, coated, non-absorbable suturing material	Braun	C0765201

(*Continued on next page*)

Continued

REAGENT or RESOURCE	SOURCE	IDENTIFIER
Abdominal open windows	Customized	N/A
Peristaltic pump	Ismatec	MS-4/8-100
Vet scan	Abaxis	VetScan VS2
Glucose meter	Roche	Accu-Chek
Accu-Chek Performa Code 222	Roche	05987270020

CONTACT FOR REAGENT AND RESOURCE SHARING

Further information and requests for resources and reagents should be directed to and will be fulfilled by the Lead Contact, Philipp Kaldis (22mtbx29@gmail.com).

EXPERIMENTAL MODEL AND SUBJECT DETAILS

Animals

Male mice of C57Bl/6J background between 8 to 9 weeks old were kept in Specific Pathogen Free (SPF) conditions. For all of the experiments, 5 siblings were kept in cages from the weaning time (21 days post-partum) until the experimental time point. All animal experiments were approved by the local veterinary authorities following guidelines from the Institutional Animal Care and Use Committee (IACUC) of the Biological Resource Center (BSF) at Biopolis in Singapore.

METHOD DETAILS

Genetic Model, and Liver and Blood Sampling

For blood tests, blood was collected by cheek punch three days before hepatectomy. At each time point after liver surgery, blood was collected by heart puncture in anesthetized mice before euthanasia. Blood tests were performed using Vetscan Comprehensive diagnostic profile (Abaxis, UK). Blood glucose was measured two hours after starvation using a glucose meter. Liver was collected and fixed in 10% NBF and paraffin and cryo blocks were prepared for histopathology analyses. *Cdk1*$^{flox/flox}$ mice were crossed with Albumin-cre mice as previously described (Diril et al., 2012). This results in hepatocyte specific deletion of *Cdk1*, which we call *Cdk1*$^{Liv-/-}$. Mice with *Cdk1*$^{+/+}$ and Albumin-cre were called WT. For hepatocytes isolation and culture, we used an inducible system: *Cdk1*$^{flox/flox}$ Albumin-creERT2 mice were called iCCH, while iWT were *Cdk1*$^{+/+}$ Albumin-creERT2. In order to induce Albumin-creERT2, we injected 5 consecutive doses of tamoxifen IP [2mg of tamoxifen (Sigma-Aldrich, T5648-5G) in corn oil (Sigma-Aldrich, C8267)]. Five days after injection, hepatocytes were harvested or 70% PHx was performed.

70% Partial Hepatectomy

Partial liver resection was performed as previously described (Mitchell and Willenbring, 2008). 8-9 weeks old mice, which received food and water ad-libitum before surgery, were anesthetized using isoflurane (1.5% pO_2) and placed on a heating pad. Once under anesthesia, a small incision of around 1 cm was done over the xiphoidal process. The liver was squeezed through the incision, and the median and left lobes were exposed and excised. After excision, muscle was sutured and the skin was closed using metal staples. Mice were humanely euthanized at the time-points of interest and liver, spleen, and other organs were collected.

Transcriptomic Analysis

Liver samples were snap-frozen in liquid nitrogen. Transcriptomic analysis was performed as previously described (Miettinen et al., 2014). Briefly, total RNA was collected using QIAzol Lysis Reagent (Qiagen) and homogenization using a Precellys homogenizer (Bertin Technologies). 15 μg of RNA was fragmented for 3 min at 70°C in RNA fragmentation buffer (Ambion). Samples were cooled on ice following addition of EDTA to 17 mM final concentration to terminate fragmentation. Tag profiling was used for transcriptomic RNAseq and the resulting library was purified with SPRI beads and sequenced at Genotypic Technology Pvt. Ltd using 54 bp single end sequencing on Illumina GAIIx. Samples obtained from 8h and 36h after PHx were sequenced using Illumina HiSeq at Edinburgh Genomics.

QTOF Metabolomic and LC/MS Analysis

Samples of 50 mg of livers were homogenized in 1.5 mL of prechilled methanol/ water (1:1) solution using a cooled TissueLyser (5000rpm, 1min with 30sec of waiting time). The supernatant was collected after centrifugation in the cold-room (4000rpm, 5 min). 650 μL was transferred and dried in a Savant speedvac at room temperature for 2h 30minutes and these were the aqueous extracts. Dried extracts were suspended in 1 ml of 25% methanol (v/v). Samples were analyzed in 1:10 dilution on a 6550 Agilent QTOF mass spectrometer by untargeted flow injection analysis as described previously (Fuhrer et al., 2011). Profile spectra with high mass accuracy were recorded from 50 to 1000 m/z in negative ionization mode. Detected ions were annotated based on

accurate mass using 5 mDa mass tolerance. Metabolites were detected using an ion-pairing ultrahigh-performance liquid chromatography–tandem mass spectrometry method as described previously (Buescher et al., 2010). Dried metabolite extracts were resuspended in 100 μl of de-ionized water and 10 μl of the precipitate free suspension were injected on a Waters Acquity UPLC system with a Waters Acquity T3 end-capped reverse-phase column (150 mm × 2.1 mm × 1.8 μm; Waters Corporation, Milford, MA, USA). Metabolites were detected and quantified on a tandem mass spectrometer (Thermo TSQ quantum triple quadrupole with electron-spray ionization, Thermo Scientific, Waltham, MA, USA) using a calibration curve of standards as well as a fully ^{13}C labelled internal standards for normalization.

Bioinformatic Analysis

We first removed the transcripts that were quantified in less than 50% of the samples across the time points and mice in WT (*Cdk1*^{WT}) and CCH (*Cdk1*$^{Liv-/-}$). We next normalized the intensity data at each time point after PHx against the basic data obtained before PHx in each mouse. We applied EBprot, a model-based method for differential gene expression analysis, to select significantly altered transcripts for all comparisons. For both types of –omics data, quantitative data were log transformed (base 2). All differential expression analysis was done using EBprot and significant findings were reported at 5% false discovery rate (FDR) throughout the manuscript (Koh et al., 2015). The gene enrichment analysis was performed using an in-house implementation for hypergeometric tests, using Gene Ontology (Ashburner et al., 2000) and ConsensusPathwayDataBase (CPDB) (Kamburov et al., 2013) as the target pathways. Heat maps were generated using the gplots library in R (http://cran.r-project.org). The list of significant transcripts and metabolites were mapped to KEGG (Kanehisa and Goto, 2000) pathways using KEGG-related utilities in R.

Intravital Imaging Using Two-Photon Microscopy Imaging

In order to use the open window imaging for TPFM, we developed a modification for the surgical resection. Briefly, we resected the superior right and left lobe accounting for 70% of the liver mass instead of the median and left lobe as previously described (Mitchell and Willenbring, 2008). Mice were anesthetized by 2% isoflurane inhalation anesthesia. An intravital imaging window chamber was installed on the abdomen as previously described (Ritsma et al., 2013). Briefly, after the midline incision through skin and ventral abdominal wall, the manubrium was clamped and removed. Next, the falciform ligament was transected to create space between the liver and diaphragm. To ensure minimal movement from respiration and a secure anatomical position of the liver, a small piece of sterile cotton was placed in the gap created by dissecting the falciform ligament. The abdominal wall and the skin were sutured using a non-absorbable 4-0 prolene purse-string suture. Next, n-butyl cyanoacrylate glue was applied to the internal or abdominal side of the imaging ring but not to the coverslip. Then the AIW was placed on top of liver. The glue firmly secured the liver to the window ring but was not in close proximity to the coverslip. Then the skin and abdominal wall were placed within the window groove and the sutures were tightened, firmly securing the window. The window chamber was fixed on the self-designed steel plate and fixed on the two-photon microscope for intravital imaging. Intravital imaging was performed with a titanium-sapphire laser (Tsunami, SpectraPhysics, Mountain View, California) with a 800 nm output. The laser was scanned using a x-y-z mirror scanning system (Model 6220, Cambridge Technology, Cambridge, Massachusetts) and guided towards the modified inverted microscope. A high-power objective (Plan Fluor ELWD water 40X, NA 0.45, Nikon) was used. Second harmonic generation signal (SHG) was obtained with a wavelength of 800 nm and detected with a 380-410 nm bandpass filter to image the collagen on the liver surface. A 410-490 nm bandpass filter isolated NADH emission and a 510-560 nm bandpass filter isolated FAD fluorescence at 800 nm excitation. Each optical scan is composed of 512 by 512 pixels and took approximately 1s to complete. Z-stack slices from liver surface to about 50μm deep at 10μm intervals were acquired. The redox ratio was calculated as previously described: the FAD image by its corresponding NADH image was divided in a chosen the region of interest. Ten pictures were taken per mouse to compare *Cdk1*$^{Liv-/-}$ to *Cdk1*^{WT} (n=3/group/time point) and from each picture we used 5 layers of depth. Each picture was split between the red channel (representing FAD autofluorescence); green channel (representing NADH); and blue channel (representing collagen). Quantification was done using ImageJ for total area of pixels as previously described.

Hepatocyte Isolation, Culture, and Immunocytochemistry

One day prior to hepatocyte isolation, tissue culture dishes were coated with collagen I (rat tail, Corning, #354236) at the same concentration as bellow. To do so, 100 μL of glacial acetic acid was diluted in 9 mL of biotechnology degree ddH_2O to a final concentration of 0.002N. Then, 1 mL of rat tail collagen type I (3.47 mg/mL, Corning® #354236) was diluted in 9 mL of the 0.002N acetic acid solution. 20μL, 40μL, or 200μL of this mix was added to each well of a Seahorse 24 XF plate, 24 well plate (Thermo Scientific, #142475) or 6 well plate (Thermo Scientific, #140675), respectively to a final amount of 3.5 μg/cm2. Once coated, plates were incubated for 12 hours at room temperature and then sealed with parafilm and stored at 4° C until used. Hepatocyte were isolated and cultured with an adaptation of the protocols published previously (Guguen-Guillouzo, 2002). For TMRE staining, following the instructions from the distributor, we stained at different cellular density and different concentrations of TMRE (tetramethylrhodamine ethyl ester, Abcam, ab113852). Primary hepatocytes were seeded at 10,000; 20,000; 40,000 and 80,000 cells per well divided in two groups; a group that received previous treatment of FCCP for 15 minutes, and a group that did not received FCCP. TMRE was titrated from 300nM, 600nM to 900nM. The best conditions for imaging TMRE in hepatocytes was when hepatocytes are seeded at 80,000 cells per well and treated with 900nM of TMRE for 30 mins.

Analysis of Hepatocytes Respiration

To study hepatocytes respiration, we used the mitochondrial stress test in a Seahorse XF24. Previous seeding, plates were coated with collagen type I (rat tail, Corning, #354236) at a concentration of 3.5 μg/cm2. Primary hepatocytes were collected from *iWT* and *Cdk1*$^{iLiv-/-}$ mice. Hepatocytes were seeded at a density of 70,000 cells/well using a Mitochondrial and Cellular Energy Phenotyping stress test in the presence of 0.5 μM of FCCP and 5 μM of oligomycin.

^{13}C-Pyruvate Metabolic Flux Analysis

^{13}C [1-13C] pyruvic acid (40 mg; Cambridge Isotope Laboratories, MA, USA, #CLM-1082-PK) mixed with 15 mM trityl radical (OXO63, GE Healthcare, Amersham UK) and 1 mM Dotarem (Guerbet, Birmingham UK), was dissolved in saline solution and polarized using a hypersense hyperpolarizer (Oxford Instruments, Oxford UK), as described previously (Lee et al., 2013). The resulting hyperpolarized [1-13C]pyruvate (0.5 mmol/kg body weight) was injected intravenously within 3 seconds and 60 individual liver spectra were acquired within 1 minute in a 9.4 T preclinical MRI scanner (Lee et al., 2013).

RNA Isolation and RT-qPCR

RNA extraction was done using the TRIzol® Reagent (Ambion™ Life technologies, #15596018) extraction protocol. The TRIzol reagent was added to liver samples (~100 mg) in 2mL Lysing Matrix D tubes (MP Biomedicals™, #6913-500). Liver samples were homogenized in a Precellys24® Dual (Bertin Technologies) cooled at 4° C using 3 cycles of 90 seconds at 5000 rpm. RNA concentration was measured using an 8-sample spectrophotometer (ND800, NanoDrop®). cDNA was prepared using Maxima® Reverse transcriptase (Fermentas Life Sciences, #EP0741) at a final concentration of 200 μg/μL total RNA. qPCR was done using the primers listed in STAR Methods using Maxima® SYBR Green qPCR Master Mix (Fermentas Life Sciences, #K0251) using 10ng of cDNA per reaction in a real-time thermal cycler (Corbett Research). *Cyclophilin A* and *E2F1* were used as normalizing genes. Analysis was done using the (2-ΔΔCt) method as previously described (Livak and Schmittgen, 2001).

Western Blotting

Liver samples (~100 mg) were lysed at 4° C in 350 μL RIPA buffer (50mM Tris pH 8.0, 0.5% sodium deoxycholate [Sigma Aldrich, D6050], 1% Nonidet P-40, 150 mM NaCl) by sonication for 15 min. Samples were transferred to a micro-centrifuge and centrifuged at 18,000 rpm for 30 minutes at 4° C. Protein quantification was performed using a colorimetric BCA Protein Assay (Thermo Scientific, #23225). 30 μg of protein lysate was separated on 12% polyacrylamide gels using Criterion™ cassettes (Bio-Rad, #345-9902) and transferred to PVDF membranes (Millipore, IPVH0010) using a semi-dry blotting system. After blotting, membranes were blocked in tris-buffered saline (t-BST) with 0.1% Tween-20 containing 5% of nonfat dry milk (Bio-Rad, #1706404). Blots were probed with the appropriate antibodies overnight at 4° C. Following primary antibody, blots were exposed to secondary goat-anti mouse or rabbit antibodies conjugated to horseradish peroxidase and developed using enhanced chemiluminescence (ECL).

AOA and Alanine Tolerance Test

Aminooxyacetic acid hemihydrochloride (AOA, Sigma, #C13408-1G) was injected using three conditions. The first condition was only one IP injection of 80mg/kilogram of mouse weight. The second condition was to reduce AOA injection to 40mg/kilogram of mouse weight and inject every day for five consecutive days. The third condition consisted of reducing the concentration of AOA to 20mg/kilogram of mouse body weight and give one injection per day for 5 consecutive days. Body weight and organ weights were collected at the end-point selected, and we observed that the third condition was the best.

Statistics

All experiments were done with a minimum of three animals. For blood tests, we used two-way ANOVA. For data that followed a normal distribution, statistical significance was tested using the two-way Student t-test, with exception in those experiments were specific statistical test is mentioned. Statistical analysis for changes in RNA expression was done using Mann-Whitney nonparametric unpaired T-test with p-value< 0.0332 (*); p-value< 0.0021 (**); p-value< 0.0002 (***); p-value< 0.0001 (****). Blood tests such as ALT, glucose and BUN was analyzed using ANOVA, with * p-value< 0.05, ** p-value< 0.005, *** p-value < 0.001. For redox ratio, and other ratios such as NAD^+/NADH and NADP/NADPH ratio, statistical analysis was done comparing WT to CCH using a multiple t-test with (n.s.) p-value>0.1234; (*) p-value≤0.0332; (**) p-value≤0.0021; (***) p-value≤0.0002; (****) p-value<0.0001. For protein western blot image quantification, statistical analysis was done using multiple t tests for group analyses with two-stage linear set-up procedure of Benjamini, Krieger and Yuketielli, with Q=1%; each of the mitochondrial component was analyzed individually without assuming consistent standard deviation; p-value > 0.1234 (n.s.); p-value≤ 0.0332 (*); p-value≤ 0.0021 (**); p-value≤ 0.0002 (***); p-value <0.0001(****). p-value of metabolic fluxes measured by functional MRI was calculated with two-tailed paired t test with 95% level of confidence, were p-value≤ 0.0332 (*); p-value≤ 0.0021 (**); p-value≤ 0.0002 (***); p-value<0.0001 (***). Finally, statistical analysis of alanine tolerance tests was done by calculating the area under the curve of each measurement; p-value was calculated with two-tailed paired t test with 95% level of confidence, were p-value≤ 0.0332 (*); p-value≤ 0.0021 (**); p-value≤ 0.0002 (***); p-value<0.0001 (***).